Ore Geology Reviews 70 (2015) 110–135

Contents lists available at ScienceDirect

Ore Geology Reviews

journal homepage: www.elsevier.com/locate/oregeorev

A new genetic model for the Triassic Yangyang iron-oxide–apatite deposit, South Korea: Constraints from in situ U–Pb and trace element analyses of accessory minerals

Jieun Seo [a], Seon-Gyu Choi [a,*], Dong Woo Kim [a], Jung Woo Park [b,c], Chang Whan Oh [d]

[a] Department of Earth and Environmental Sciences, Korea University, Seoul 136-701, South Korea
[b] Research School of Earth Sciences, Australian National University, Canberra, ACT 2612, Australia
[c] School of Earth and Environmental Sciences/Research Institute of Oceanography, Seoul National University, Seoul 151-747, South Korea
[d] Department of Earth and Environmental Sciences, Jeonbuk National University, Jeonju, South Korea

ARTICLE INFO

Article history:
Received 23 January 2015
Received in revised form 3 April 2015
Accepted 7 April 2015
Available online 10 April 2015

Keywords:
Yangyang
IOA deposit
LA-ICP-MS U–Pb apatite and sphene dating
SHRIMP U–Pb zircon dating
Korea

ABSTRACT

The Yangyang iron-oxide–apatite deposit in South Korea has undergone multiple episodes of igneous activity, deformation, hydrothermal alteration, and iron-oxide–apatite (IOA) mineralization. The iron orebodies occur as concordant- to discordant-layered lenticular or massive magnetite and/or magnetite–pyrite ores. The iron mineralization occurs along a N–S-trending shear zone within the Yangyang syenite, which experienced both early ductile and later brittle deformations. Alteration was caused mainly by the injection of hydrothermal fluid through the shear zone, leading to Fe–P mineralization. We recognize multiple stages of alteration in the Yangyang deposit, based on a paragenesis that is defined by distinct mineral assemblages including Na–Ca–K alteration phases (e.g., albite, diopside, actinolite, and biotite) and accessory minerals containing high field strength elements (e.g., apatite, sphene, allanite, and monazite). The alteration around the magnetite ore body shows an evolutionary trend from Ca (–Na) alteration, through K to phyllic alterations. The Fe–P mineralization is associated with the Ca–K and K alteration products. The iron orebodies are hosted by deformed and altered syenite, which intruded the Paleoproterozoic gneiss complexes at 233 ± 1 Ma (SHRIMP U–Pb zircon age) in a post-collisional tectonic setting. LA-ICP-MS U–Pb dating of REE-rich sphene and apatite from the iron ores and alteration products yields Fe mineralization ages of 216 ± 3 Ma (sphene) and 212 ± 13 Ma (apatite). This is the first time, which IOA-type mineralization in the Korean Peninsula was dated as Triassic age related to post-collisional magmatism within the Gyeonggi Massif, South Korea. The U–Pb system was subsequently reset (208 ± 3 Ma–sphene and 151 ± 13 Ma–apatite) by Jurassic and Cretaceous magmatism. This unique geological evolution was responsible for Mesozoic metal enrichment and remobilization into suitable structural traps in the Yangyang district.

1. Introduction

The Yangyang magnetite–apatite deposit is one of the largest iron deposits in South Korea (Fig. 1). The deposit has produced about eight million metric tons of ore with an average iron content of ~60 wt.%, and without economic copper and gold production (Choi et al., 2004). Because of its complex occurrence, the processes that formed the Yangyang magnetite–apatite deposit have remained controversial for 50 years. Lee (1968) argued that the deposit was formed by metasomatism following intrusion of iron-oxide magma into a metasedimentary sequence. Kim et al. (1958) and James et al. (2005) argued that the iron mineralization in this area resulted from contact metasomatism or skarnification. Other researchers have suggested that the deposit represents metamorphosed iron-rich calcareous sediments (So, 1978; So et al., 1975), alkali metasomatized meta-sediments, or regionally metamorphosed iron-rich calcareous sedimentary rocks (Kim, 1977; Lee, 1987; Lee and Kim, 1968; Lee and Stout, 1989). The variety of genetic models reflects the complex geology of the Yangyang deposit. The region experienced multiple stages of regional metamorphism, magmatism, deformation, hydrothermal alteration, and mineralization during the Mesozoic (Choi et al., 2011). This history resulted in a complex juxtaposition by shearing of different lithological units, ages, deformation characteristics, and hydrothermal alteration features. No previous genetic model of the Yangyang deposit has incorporated a systematic investigation of the geochemical, geochronological, and structural characteristics of the deposit, even though structural and lithological controls generally play an important role in iron-oxide–copper–gold (IOCG)/iron-oxide–apatite (IOA)-type mineralization (Duncan et al., 2014; Valley et al., 2011; Williams et al., 2005).

* Corresponding author.
E-mail address: seongyu@korea.ac.kr (S.-G. Choi).

http://dx.doi.org/10.1016/j.oregeorev.2015.04.009
0169-1368/

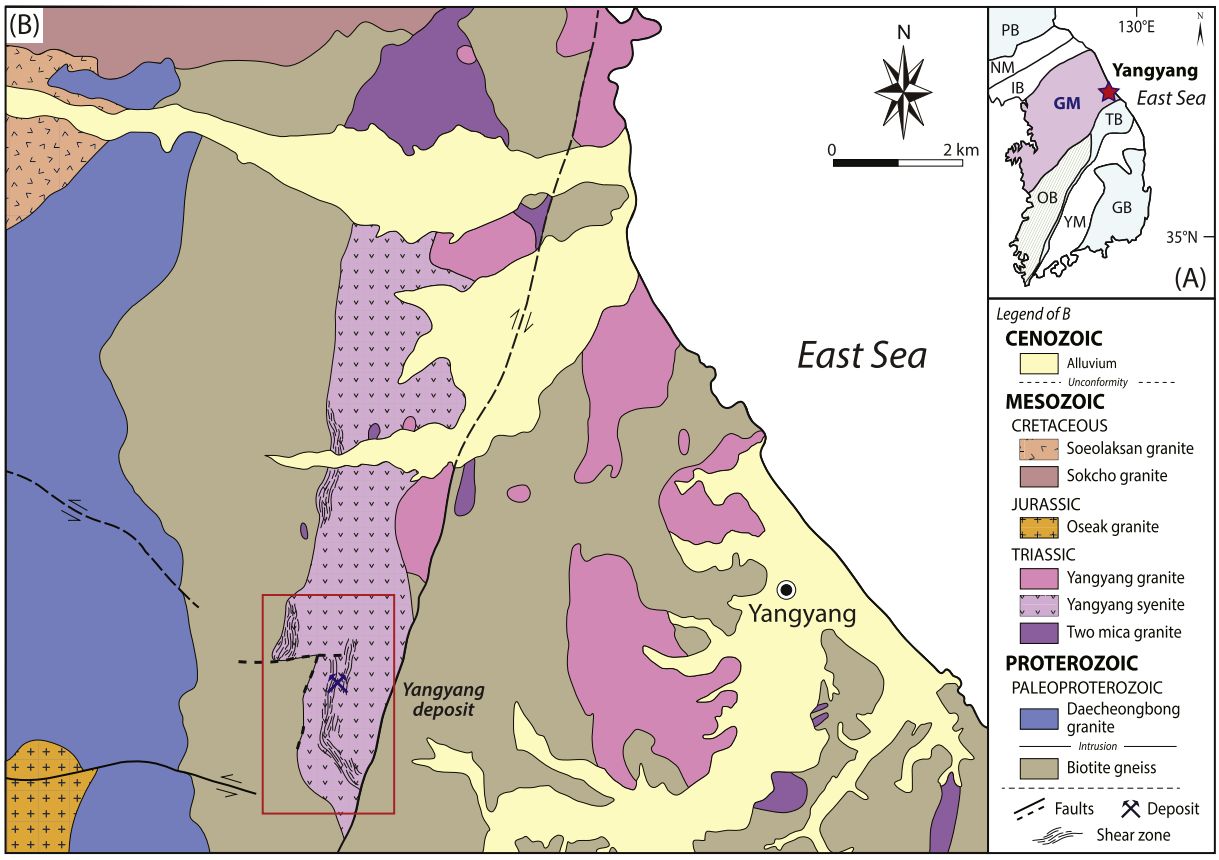

Fig. 1. Simplified regional geological map of the Yangyang area in South Korea. The red box indicates the area shown in Fig. 3. (For interpretation of the references to color in this figure legend, the reader is referred to the web version of this article.)

The petrology of the deformed and altered syenite that is closely associated with the iron mineralization, and the origin of the abundant phosphate minerals such as apatite, have received little attention.

In this study we measured the major and trace element concentrations, and U and Pb isotopic compositions of the magnetite, apatite, sphene, and zircon from the Yangyang deposit. We use these data, along with the petrology and whole-rock geochemistry of the syenite and iron ore, to investigate the ages of emplacement, deformation, and hydrothermal alteration of the syenite, and the age and ore-forming processes of the Yangyang deposit. We also reconstruct the temporal, spatial, structural, and genetic relationships among Triassic syenite magmatism, IOA-type mineralization, and hydrothermal alteration.

2. Geologic setting

The Precambrian Gyeonggi Massif is located between the Imjingang and Okcheon metamorphic belts on the Korean Peninsula (Fig. 1A). The Yangyang deposit is located at the southeastern margin of the Gyeonggi Massif (Fig. 1B) and is surrounded by country rock consisting of Paleoproterozoic biotite gneiss (Fig. 2A) and the Daecheongbong granite. The Paleoproterozoic rocks are intruded by the Triassic Yangyang syenite (Fig. 2B), the Yangyang biotite granite, and two-mica granite, as well as the Jurassic Oseak granite and the Cretaceous Sokcho and Seolaksan granites (Fig. 1B; Kim, 2014; Song et al., 2011). SHRIMP U–Pb zircon dating shows that the Yangyang granite was emplaced at 228.8 ± 2.2 Ma, which is broadly contemporaneous with the 230 ± 2 Ma Yangyang syenite (Song et al., 2011; Fig. 1B). The Yangyang syenite is considered to have been emplaced in the Gyeonggi Massif during widespread Triassic post-collisional magmatism (Oh et al., 2006; Seo et al., 2010).

The alteration and Fe mineralization of the Yangyang deposit developed along an approximately 200-m-wide N–S-trending elongate mylonitic shear zone within the syenite intrusion (Figs. 1B, 2C, 3). About 20 discrete magnetite orebodies occur in the Domok, Yangyang, Yangnon, and Nonhwa deposits (Fig. 2). The orebodies are located within calcic–potassic and potassic alteration zones, along or adjacent to the shear zone. The fresh (massive) syenite is not associated with iron mineralization.

2.1. Host rock

The Middle Triassic Yangyang syenite, which intruded Paleoproterozoic biotite gneiss, has an E–W extent of 2 km and a N–S extent of 10 km, and is located west of Yangyang City in the southeastern part of the Gyeonggi Massif (Fig. 1B). Lee and Kim (1968) subdivided the Yangyang syenite into porphyritic gneissic syenite, porphyritic massive syenite, gneissic syenite, and massive syenite on the basis of texture; however, we classify the syenite, based on the degree of alteration and deformation textures, into syenite, mylonitic syenite, and cataclastic syenite. Most of the syenite intrusion is foliated, with some undeformed massive syenite located in the central and southwestern parts of the syenite body. Mylonitic and cataclastic syenites occur in the shear zone within the foliated syenite (Figs. 2, 3). The syenite is composed mainly of K-feldspar (40–60 vol.%), amphibole (5–30 vol.%), plagioclase (20–25 vol.%), biotite (5–10 vol.%), quartz (<5 vol.%), and accessory minerals including apatite, sphene, magnetite, and zircon. The syenite typically contains lath-shaped K-feldspar phenocrysts of 1–3 cm in length (Fig. 4A). These phenocrysts are commonly pinkish owing to prophylitic alteration (Fig. 4F). The mylonitic syenites have been both altered and deformed, and have a protomylonitic to mesomylonitic texture (Figs. 4B, C, and 5A). The protomylonitic syenites have elongate K-feldspar grains or aggregates (Fig. 4B), whereas the mesomylonitic

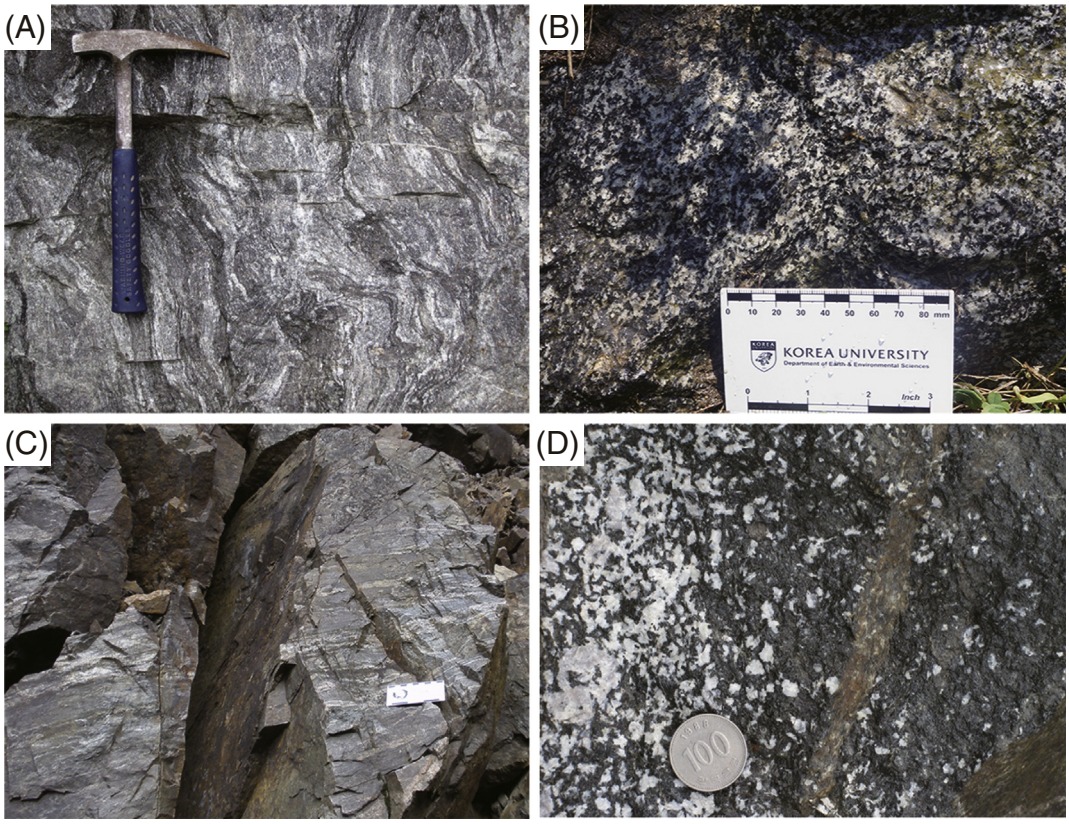

Fig. 2. Field photos of host and deformed or altered rocks. (A) Precambrian gneiss. (B) Massive syenite. (C) Mylonitic syenite in a shear zone, which resembles metasedimentary rocks or gneiss resulting from strong deformation. (D) Continuous change from syenite to altered syenite. The left part of the photo shows an original igneous feldspar grain, while on the right photo the original texture has been altered to resemble amphibolite by Ca alteration.

syenites are strongly deformed and have a gneissic texture (Figs. 4C, 5A). The cataclastic syenites contain relatively unaltered crushed grains of various sizes (from ~1 mm to 3 cm) (Fig. 4D, E). Some cataclastic syenites contain brittle-fractured K-feldspar with mafic minerals and mafic mineral veins formed among the clasts (Fig. 4D). The Yangyang granite consists mainly of K-feldspar, quartz, plagioclase, biotite, and minor amphibole, apatite. Some K-feldspars are partly sericitized.

2.2. Structural relationships and deformation history

The close spatial association of the Yangyang deposit iron mineralization with the shear zone implies that the regional structure played an important role in the mineralization. The major structural features in this area are NNE–SSW and E–W-trending faults, and N–S-trending shear zones (Figs. 1, 2). A N–S-trending extensional shear zone (5–6 km wide) is developed within the Yangyang syenite (Fig. 1), and the shear zone contains mylonite that has obliterated the original porphyritic texture of the syenite. Cataclastic syenite subsequently formed along the shear zone by brittle reactivation of ductilely-deformed syenite during exhumation. The resulting cataclastic overprint of mylonitic textures in the syenite is visible at macroscopic and microscopic scales (Figs. 4D, 5B). The undeformed and cataclastic syenite underwent prophylitic alteration, whereas multiple episodes of hydrothermal alteration enriched the mylonitic syenite in Na, Ca, K, and Fe. After brittle and/or ductile deformation, the hydrothermal alteration gradually destroyed the original igneous textures of strongly altered syenites, leaving a dark greenish rock with a mafic appearance (Fig. 2D). These orebodies occur along the shear zone, within the Yangyang syenite. The high-grade ores generally occur in highly brecciated areas as lenses that are elongate parallel to the N–S-trending shear zones (Fig. 3). Stretching lineations record the dip-slip fault movement that generated the gently plunging ore body shape.

2.3. Hydrothermal alteration and mineralization

Large-scale hydrothermal alteration occurs along the shear zones in the Yangyang area (Fig. 1B). We identified several main alteration events affecting the Yangyang syenite, and we divide them into Ca (–Na), Ca, Ca–K, K, and phyllic alterations on the basis of characteristic mineral assemblages. These alterations occurred under conditions close to those of the brittle–ductile transition. Secondary alteration minerals such as albite, amphibole, and biotite are indicative of Na, Ca, and K alteration, respectively. The early sodic alteration was weak, occurred throughout a broad area within the Yangyang syenite, and was extensively overprinted by calcic and later potassic alteration. Areas of Fe–P mineralization are strongly associated with Ca–K and K alteration zones near the center of the shear zone. An extensive Ca alteration zone reveals that the Ca was sourced from multiple fluids that in turn were derived from hidden magmatic sources along the zone of structural weakness.

The early Ca (–Na) alteration formed albite, clinopyroxene, amphibole, apatite, sphene, and minor biotite. The presence of secondary albite indicates pervasive sodic alteration in the study area. The foliation in the Ca (–Na)-altered mylonitic syenites consists of alternating millimeter-scale layers of mafic and felsic minerals. The felsic domains are composed of fine-grained plagioclase with albite twins and apatite, whereas the mafic domains contain medium-grained amphibole with minor clinopyroxene, epidote, allanite, sphene, and sericite (Fig. 5C).

Ca-rich mineral assemblages have strongly overprinted the early sodic alteration, resulting in a Ca-altered syenite consisting mainly of magnetite, amphibole, clinopyroxene relicts, sphene, apatite, epidote, K-feldspar and albite, with minor allanite and zircon (Figs. 4G, 5D). Two altered samples (YY1003-16 and YY1003-18) have anomalously high concentrations of sphene (5–10 vol.%) as a result of Ca alteration.

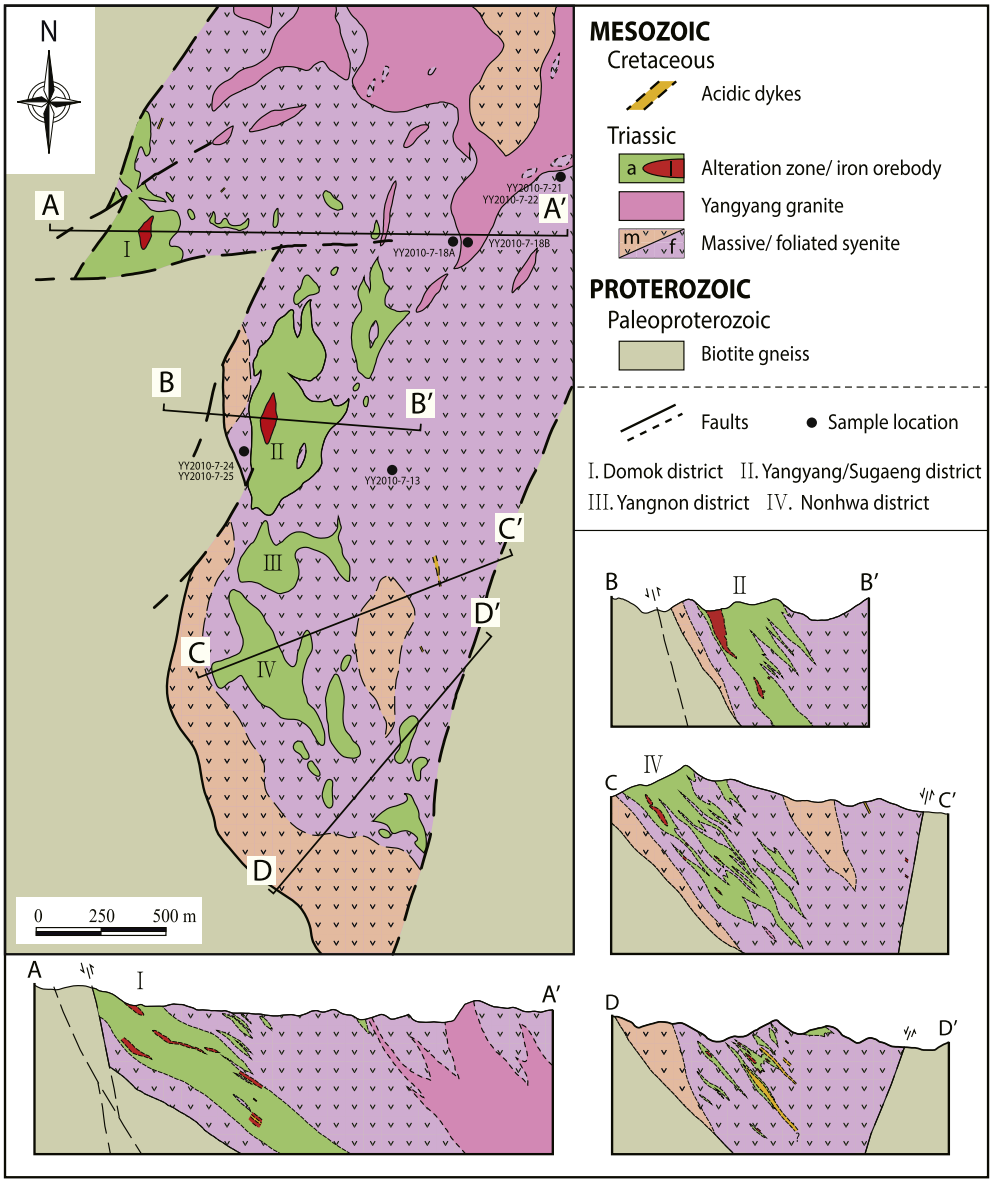

Fig. 3. Detailed geological map and cross-sections (A–A′ to D–D′) of the Yangyang ore deposit in South Korea modified from KORES (2010). For the location, see Fig. 1.

The Ca–K alteration is evident by a mineral assemblage consisting of magnetite, amphibole, biotite, sphene, apatite, and K-feldspar, with minor quartz, sericite, allanite, zircon, and rutile (Fig. 5E). The Ca–K alteration products are dark green to black, and their original igneous textures have been obliterated by structural deformation and chemical alteration. They contain fractured plagioclase crystals, which display albite twinning and are sericitized, and disseminated anhedral sphene and apatite. Amphiboles are cut by biotite veinlets, which indicate that K alteration overprinted the Ca alteration. Fine-grained biotite also fills the interstitial spaces between crushed amphibole and plagioclase, or replaces amphibole.

Original mineral assemblages were not observed macroscopically in the K alteration products because of strong deformation and chemical alteration (Figs. 4H, 5E). Most apatites are anhedral and <1 mm in size, and sphene is rare in the K alteration products. Locally, zones of phyllic alteration still show the original igneous texture along with some fracturing of grains and alteration (Fig. 4I). The K alteration zone commonly consists of magnetite, biotite, apatite, K-feldspar, plagioclase, muscovite, sericite, epidote, and quartz, with minor pyrite, hematite, and carbonates. Most K-feldspar and plagioclase grains have been micro-fractured and sericitized, and a few plagioclase grains display albite twins.

Iron mineralization occurs as concordant to discordant layered, lenticular or massive ores that can be subdivided into two main types: magnetite ore and magnetite–pyrite ore. The magnetite ore is typically composed of magnetite, amphibole, biotite, apatite, and sphene, along with minor albite, K-feldspar, diopside, fluorite, sericite, epidote, allanite, zircon, carbonates, and sulfides. The magnetite–pyrite ore typically consists of magnetite, pyrite, apatite, sphene, amphibole, biotite, chlorite, muscovite, monazite, carbonates, and sulfides (Figs. 4J, 5G). The association of magnetite ores with amphibole, sphene, biotite, fluorapatite, and muscovite indicates that the iron mineralization was mainly related to Ca–K and/or K alterations along the shear zone. The magnetite–pyrite ores have relatively high concentrations of apatite compared with the magnetite ores (Fig. 5H). The sulfides in the magnetite ore and in magnetite–pyrite ore, which consist of pyrite with minor pyrrhotite, sphalerite, and chalcopyrite, clearly represent a late-stage overprint on the early iron-oxide stage assemblages. Some

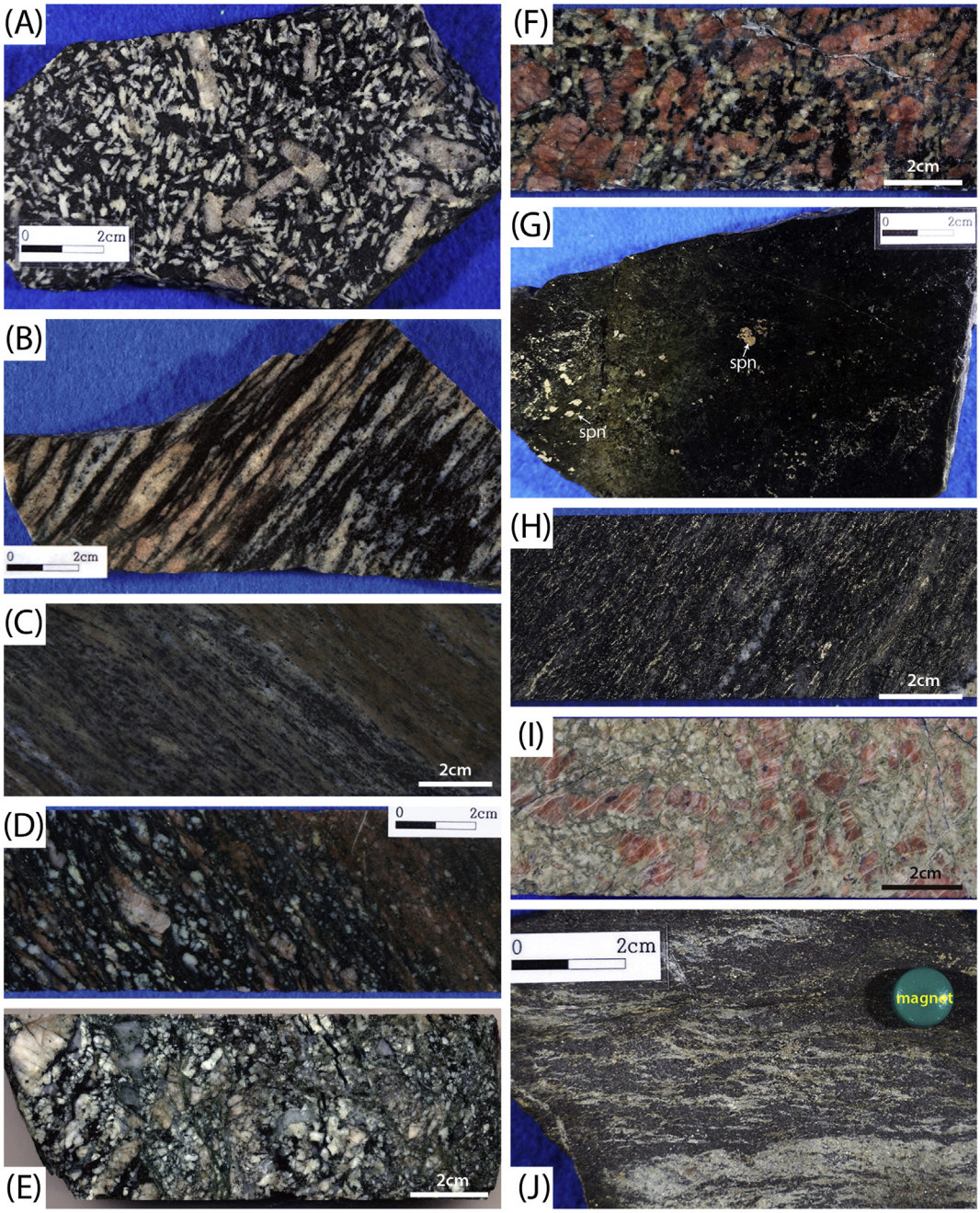

Fig. 4. Photographs of representative polished hand specimens of Triassic syenite and altered rocks from the Yangyang area. (A) Yangyang syenite showing prismatic feldspar crystals. (B) Feldspar augen in a foliated mylonitic syenite. (C) This mesomylonitic syenite resembles gneiss, with its elongate mafic minerals. (D) Cohesive brecciated feldspar with a foliation defined by the preferred orientation of fine-grained mafic minerals. (E) Brecciated feldspar in cataclastic syenite, showing the in situ fracturing of grains. (F) Most syenite underwent prophylitic alteration without physical deformation. (G) Ca alteration products with fine- to medium-grained sphene. (H) K alteration products are difficult to identify with the naked eye, although the mineral texture can be discerned. (I) Phyllic alteration. (J) Layer of magnetite–pyrite ore showing alteration minerals such as biotite. Abbreviation: spn—sphene.

apatites contain solid-bearing fluid inclusions such as halite, sylvite, pyrite, and chalcopyrite (Fig. 6). The halite-bearing fluid inclusions in the apatite indicate that the hydrothermal system evolved from saline fluids.

3. Analytical methods

Whole-rock major, trace, and rare earth element (REE) concentrations were determined using inductively coupled plasma-atomic emission spectrometry (Termo JarrelAsh ENVIRO II), inductively coupled plasma-mass spectrometry (Perkin Elmer Optima 3000), and instrumental neutron activation analysis at Activation Laboratories Ltd., Canada. Representative whole-rock elemental concentrations of the Yangyang syenites, cataclastic syenites, and granites are presented in Table 1, and for mylonitic syenites and altered rocks in Table 2.

Zircons were separated from sample YY110715-1 of the undeformed Yangyang syenite by crushing, water-based panning, and magnetic techniques. Hand-picked zircon grains were then mounted in epoxy along with chips of reference zircons FC1 (Duluth gabbro) and SL13 (Sri Lankan gem). The mounts were polished to reveal cross-sections through the centers of the grains. The Pb–U–Th isotope concentrations of the zircons were analyzed using a SHRIMP II ion microprobe housed

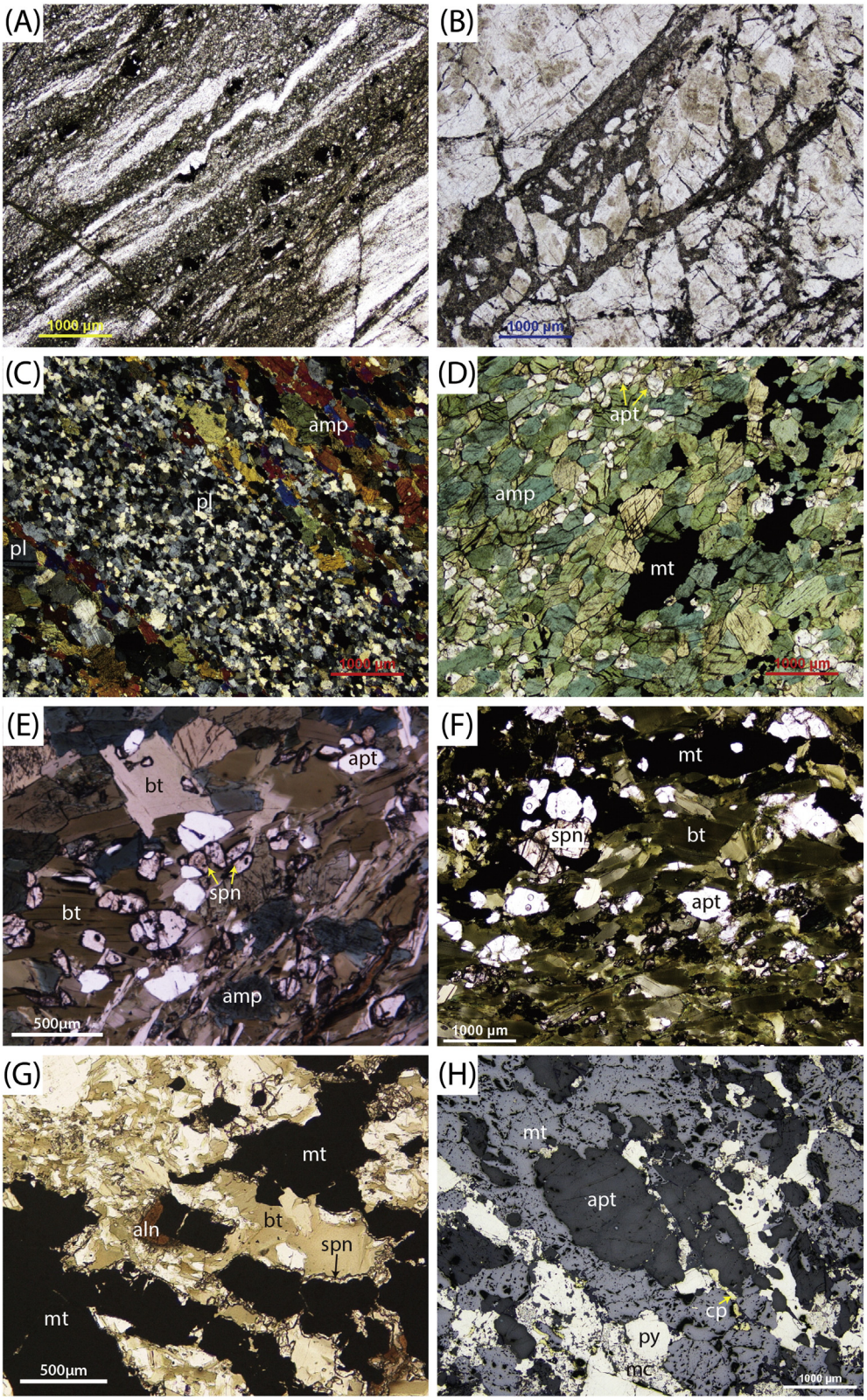

Fig. 5. Photomicrographs of host rocks from the Yangyang area (A–G: plane polarized light, H: reflected light). (A) Foliation in mylonitic syenite. (B) Brecciated feldspars in cataclastic syenite. (C) Ca (–Na) alteration products. (D) Ca alteration products. (E) Ca–K alteration products. (F) K alteration products. (G) Magnetite ore. (H) Magnetite–pyrite ore. Abbreviations: aln—allanite; amp—amphibole; apt—apatite; bt—biotite; cp—chalcopyrite; mc—marcasite; mt—magnetite; pl—plagioclase; py—pyrite; spn—sphene.

at the Korea Basic Science Institute (KBSI) in Ochang, South Korea. For details of the standard operating techniques, see Miao et al. (2002). Instrumental conditions and data acquisition procedures were similar to those described by Williams (1998). Circular to oval areas of 20–25 μm across were analyzed on morphologically distinct domains selected from cathodoluminescence (CL) images. Each U–Pb analysis

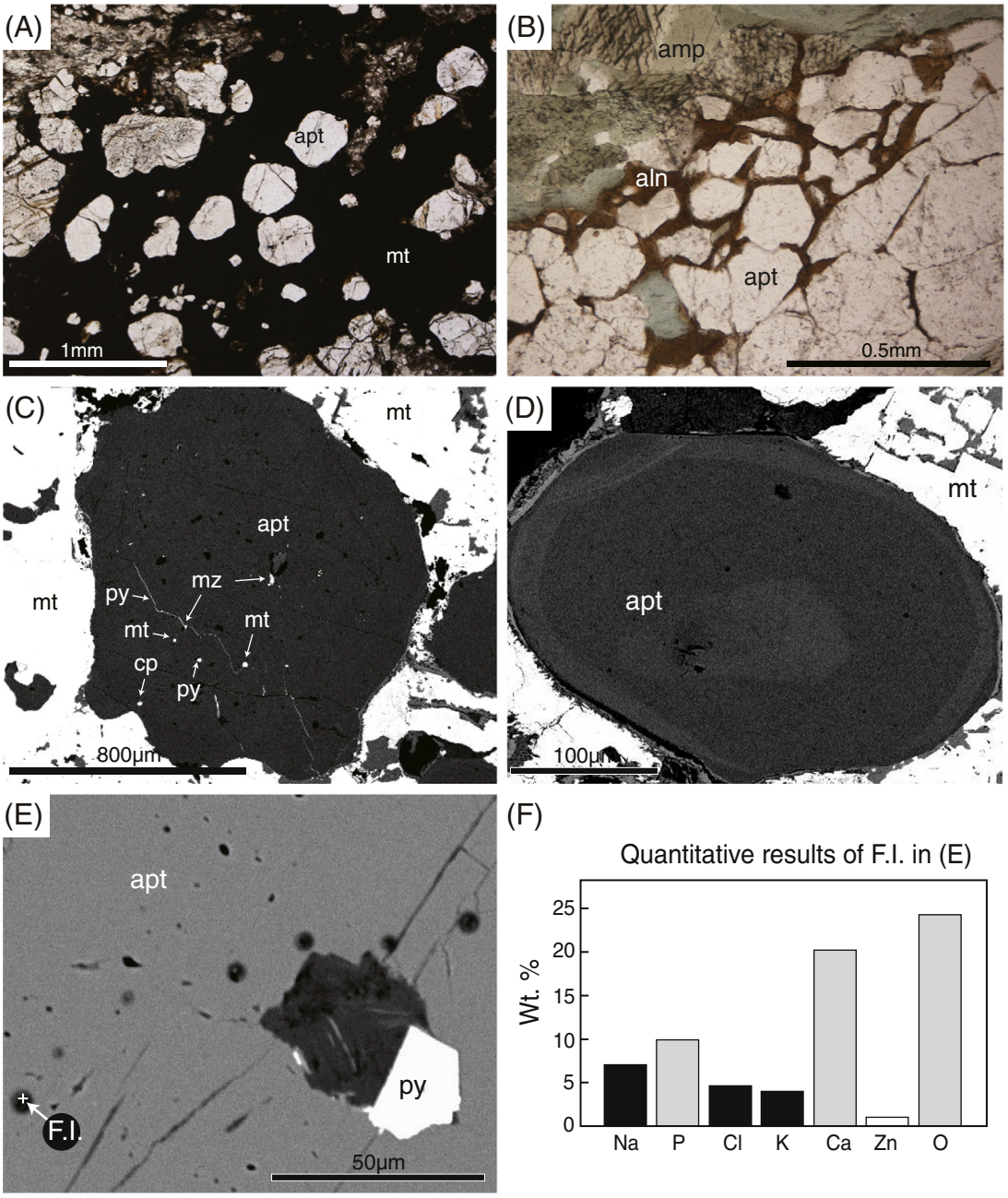

Fig. 6. Types of apatite. (A) Type-I apatite and magnetite within the magnetite–pyrite ore. (B) Type-II apatite mainly mantled by late stage allanite. (C) Type-Ia apatite contains many inclusions such as magnetite, pyrite, monazite and chalcopyrite. (D) Relatively fine-grained Type-Ib apatites contain no inclusions. (E) Type-Ia apatite contains numerous fluid inclusions. (F) Quantitative analyses of fluid inclusions within the Type-Ia apatite of (E) detected Na, Cl, and K as well as apatite components (Ca, P, and O). Abbreviations: F.I.—fluid inclusion; aln—allanite; amp—amphibole; apt—apatite; bt—biotite; mt—magnetite; mz—monazite; spn—sphene.

consisted of five scans through the mass range. The data were reduced according to the method of Williams and Claesson (1987) and Williams (1998) using the SQUID Excel Macro of Ludwig (2000). Ages were calculated using constants recommended by the International Union of Geological Sciences (IUGS) Subcommission on Geochronology (Steiger and Jäger, 1977). Results are listed in Table 3.

Mineral compositions were determined using an electron microprobe (JEOL JXA-8600 SX) with energy dispersive spectroscopy (INCA-6025, Oxford Instruments) at Korea University, Seoul, South Korea. The microprobe was operated with an accelerating voltage = 15.0 kV, beam current = 3.0 nA, live time = 100 s, and probe diameter = 3 μm. Results are listed in Table 4.

Trace elements of sphene and apatite were determined using laser ablation-inductively coupled plasma-mass spectrometry (LA-ICP-MS) at the Research School of Earth Science, Australian National University (ANU), Canberra, Australia. The system consists of an excimer laser (Compex 110, Lambda Physik) operating with an Ar–F mixture at λ = 193 nm and coupled to an ICP-MS (Agilent 7700). He and Ar were used as the ablation gas medium via an ANU-designed HelEx ablation cell. The LA-ICP-MS analyses were performed using a laser pulse rate of 5 Hz and spot size of 47 μm. An external glass standard (NIST 610) was used to correct for yield differences in trace elements. ^{43}Ca obtained from the electron microprobe analysis was employed as an internal standard. Data reduction was performed using an in-house

Table 1
Representative whole-rock chemical compositions of the syenite in the Yangyang area, South Korea.

Rock type	Syenite					Cataclastic syenite										Yangyang granite	
Sample	Y16	Y38	YY110715-1	YY2010-7-24	YY201306-3-1	Y24	YY1001-1	YY1105-8C	YY1105-8D	YY1105-8E	YY2010-7-13	YY2010-7-18A	YY2010-7-21	YY2010-7-22	YY2010-7-25	YY-GR	YY2010-7-18B
Major elements (wt.%)																	
SiO_2	60.84	61.67	56.72	52.42	56.42	56.54	54.84	58.88	56.85	58.14	56.63	54.82	56.60	56.23	53.07	63.49	63.54
Al_2O_3	15.71	14.46	15.8	16.91	16.98	14.40	16.62	15.55	16.98	16.89	15.52	16.02	15.89	15.96	16.92	16.59	14.66
$Fe_2O_3^{tot}$	5.97	5.76	6.61	8.32	7.35	8.55	7.26	6.51	7.05	7.34	6.25	7.10	6.96	6.74	7.60	5.26	5.66
MnO	0.09	0.14	0.128	0.14	0.12	0.16	0.12	0.09	0.10	0.09	0.19	0.12	0.11	0.12	0.13	0.08	0.10
MgO	2.89	2.13	3.31	4.28	3.95	3.90	3.51	2.90	3.15	3.22	3.92	3.88	3.72	3.51	3.90	1.47	2.72
CaO	4.30	3.93	5.15	6.37	6.09	6.07	5.80	3.19	3.38	3.03	5.52	5.17	4.26	5.34	5.79	4.74	3.37
Na_2O	3.69	3.45	3.33	3.67	3.69	4.22	3.89	3.25	3.56	3.79	4.38	3.05	3.78	3.59	3.20	3.30	3.62
K_2O	4.37	6.66	4.27	4.09	3.79	3.18	4.00	5.33	4.98	4.21	4.49	5.34	4.70	4.42	5.11	2.50	3.18
TiO_2	0.71	0.41	0.75	1.03	0.98	1.19	0.85	0.68	0.77	0.71	0.75	0.90	0.92	0.91	0.97	0.64	0.51
P_2O_5	0.35	0.28	0.42	0.56	0.47	0.51	0.46	0.29	0.38	0.38	0.46	0.47	0.47	0.45	0.51	0.16	0.36
LOI	0.89	1.69	2.24	1.53	0.99	1.11	1.01	2.31	3.67	2.99	0.97	3.31	2.57	1.80	2.40	0.70	2.02
Total	99.83	100.60	98.28	99.31	100.80	99.84	98.36	98.99	100.90	100.80	99.08	100.20	99.99	99.07	99.61	98.92	99.74
$Na_2O + K_2O$	8.06	10.11	7.60	7.76	7.48	7.40	7.89	8.58	8.54	8.00	8.87	8.39	8.48	8.01	8.31	5.80	6.80
Mg#	49.0	42.3	49.8	50.5	51.6	47.5	48.9	46.9	47.0	46.5	55.4	52.0	51.4	50.8	50.4	35.6	48.8
Trace and rare earth elements (ppm)																	
Sc	10	12	16	18	16	14	16	11	14	15	14	16	15	13	14	9	17
Be	4	3	5	4	3	4	4	3	3	4	7	4	4	4	3	2	5
V	87	79	116	149	125	123	125	84	95	95	99	124	118	118	131	63	86
Cr	70	40	60	90	100	80	70	60	70	70	80	90	80	62	65	b.d.	60
Co	12	9	12	17	14	17	14	12	12	13	16	15	15	14	16	8	11
Ni	27	14	b.d.	b.d.	20	22	b.d.	b.d.	b.d.	b.d.	b.d.	b.d.	b.d.	19	19	b.d.	b.d.
Cu	12	3	10	10	20	2	20	40	40	20	b.d.	10	b.d.	12	7	b.d.	b.d.
Zn	71	82	90	130	90	146	80	70	90	100	170	120	120	84	85	70	110
Ga	22	18	21	25	21	21	25	19	23	25	26	23	22	23	23	21	22
Ge	1.6	1.8	1.7	1.9	1.3	1.7	1.5	1.6	1.6	2.3	1.9	2.0	1.7	2.1	1.9	b.d.	1.9
As	b.d.	b.d.	b.d.	b.d.	b.d.	b.d.	b.d.	b.d.	b.d.	b.d.	b.d.	b.d.	b.d.	b.d.	b.d.	b.d.	b.d.

(continued on next page)

Table 1 (*continued*)

Rock type	Syenite					Cataclastic syenite										Yangyang granite	
Sample	Y16	Y38	YY110715-1	YY2010-7-24	YY201306-3-1	Y24	YY1001-1	YY1105-8C	YY1105-8D	YY1105-8E	YY2010-7-13	YY2010-7-18A	YY2010-7-21	YY2010-7-22	YY2010-7-25	YY-GR	YY2010-7-18B
Rb	122	136	118	133	104	63	118	125	139	130	110	140	141	86	141	92	114
Sr	946	564	1054	1188	1124	637	1113	916	917	1140	533	1060	912	1057	1281	500	858
Y	23.1	21.5	30.0	26.8	23.0	20.0	23.5	25.2	30.1	32.0	52.7	27.0	27.5	29.4	25.4	13.7	26.0
Zr	293	169	258	371	311	431	316	227	317	316	338	319	325	301	321	301	176
Nb	36.2	22.4	32.4	30.4	19.2	45.7	30.2	27.2	26.4	20.6	83.4	29.7	33.6	38.6	32.9	7.6	18.0
Mo	b.d.	b.d.	b.d.	b.d.	b.d.	b.d.	b.d.	b.d.	b.d.	b.d.	b.d.	b.d.	b.d.	b.d.	b.d.	b.d.	b.d.
Ag	b.d.	b.d.	0.6	0.8	0.8	b.d.	0.5	1.3	2.0	1.9	0.9	0.8	0.8	b.d.	b.d.	2.7	0.5
In	b.d.	b.d.	b.d.	b.d.	b.d.	b.d.	b.d.	b.d.	b.d.	b.d.	b.d.	b.d.	b.d.	b.d.	b.d.	b.d.	b.d.
Sn	3	7	4	3	2	4	3	3	6	5	8	3	3	3	2	b.d.	4
Sb	b.d.	b.d.	b.d.	0.5	b.d.	b.d.	0.3	b.d.	b.d.	b.d.	0.4	0.4	0.4	b.d.	0.4	b.d.	0.4
Cs	3.3	0.7	1.6	2.2	1.8	0.2	1.8	1.3	2.7	4.8	1.1	3.1	3.1	1.0	1.6	1.9	2.0
Ba	1784	2753	1647	1821	2001	1993	1939	2143	2357	1803	2097	2345	1877	1787	2525	683	1087
La	87.8	86.0	46.9	57.5	60.0	64.1	60.7	72.4	87.5	79.5	99.6	59.6	56.2	70.1	52.8	85.1	110.0
Ce	160.0	115.0	100.0	116.0	110.0	110.0	109.0	135.0	153.0	136.0	189.0	120.0	113.0	142.0	103.0	143.0	186.0
Pr	15.6	10.2	11.8	12.9	12.6	10.5	12.2	14.7	15.7	14.1	20.2	13.1	12.5	15.7	11.5	13.8	17.9
Nd	54.3	36.8	46.3	50.1	45.9	40.0	48.0	53.8	55.6	50.1	77.2	51.0	47.7	60.9	46.0	45.9	60.6
Sm	8.08	6.52	8.75	9.78	7.97	6.87	8.69	9.20	9.39	9.15	14.70	9.39	8.71	10.90	8.77	6.34	10.90
Eu	2.11	1.51	2.10	2.59	2.34	2.27	2.49	2.17	2.23	2.03	2.93	2.55	2.32	2.60	2.47	1.44	1.75
Gd	6.19	5.28	6.39	7.47	6.18	5.75	6.88	5.94	6.85	7.07	11.80	7.38	6.99	8.17	7.01	4.88	7.91
Tb	0.83	0.78	0.96	1.07	0.90	0.78	0.97	0.89	0.99	1.04	1.79	1.07	1.02	1.15	0.98	0.50	1.10
Dy	4.43	4.26	5.43	5.63	4.62	4.05	5.10	4.66	5.36	5.75	9.83	5.65	5.33	6.15	5.26	2.58	5.77
Ho	0.84	0.82	1.05	1.00	0.86	0.75	0.99	0.90	1.04	1.13	1.90	1.06	0.98	1.13	0.94	0.47	1.03
Er	2.49	2.37	2.95	2.77	2.30	2.08	2.62	2.48	2.89	3.03	5.51	2.93	2.90	3.17	2.58	1.32	2.72
Tm	0.40	0.34	0.43	0.39	0.32	0.30	0.38	0.36	0.43	0.41	0.82	0.41	0.44	0.45	0.38	0.19	0.36
Yb	2.56	2.11	2.86	2.52	2.02	1.99	2.43	2.32	2.56	2.48	5.31	2.59	2.95	2.75	2.44	1.34	2.15
Lu	0.364	0.305	0.464	0.403	0.290	0.310	0.366	0.361	0.379	0.357	0.842	0.405	0.466	0.419	0.381	0.231	0.318
Hf	7.1	3.8	5.6	7.8	5.9	8.8	6.9	5.8	7.3	7.3	7.7	7.1	7.4	6.8	6.9	6.9	4.4
Ta	3.35	1.72	2.36	1.33	1.04	2.19	3.92	1.54	1.41	0.99	6.79	1.66	1.57	2.02	1.29	0.70	0.86
W	b.d.	b.d.	0.6	0.8	b.d.	b.d.	b.d.	1.6	1.1	0.8	1.0	0.6	b.d.	0.8	1.1	b.d.	0.8
Tl	0.5	0.4	0.6	0.6	0.6	0.2	0.6	0.7	0.7	0.8	0.3	0.6	0.7	0.4	0.5	0.5	0.6
Pb	22	17	22	17	18	20	19	20	13	14	67	31	22	20	21	23	18
Bi	0.1	0.3	b.d.	b.d.	0.2	0.1	b.d.	b.d.	b.d.	b.d.	0.7	0.1	b.d.	0.1	0.1	b.d.	b.d.
Th	16.3	9.6	5.7	2.5	6.2	6.4	8.0	9.6	11.6	10.4	13.0	8.0	8.0	10.4	3.4	23.2	18.2
U	3.78	1.80	2.19	0.82	1.21	2.97	2.28	1.92	1.91	1.39	4.30	2.67	2.02	2.64	1.27	2.32	2.40
$\sum$REE	346.0	272.3	236.4	270.1	256.3	249.8	260.8	305.2	343.9	312.1	441.4	277.1	261.5	325.6	244.5	307.1	408.5
Eu/Eu*	0.91	0.79	0.86	0.93	1.02	1.10	0.98	0.90	0.85	0.77	0.68	0.94	0.91	0.84	0.96	0.79	0.58
La_N/Yb_N	24.6	29.2	11.8	16.4	21.3	23.1	17.9	22.4	24.5	23.0	13.5	16.5	13.7	18.3	15.5	45.6	36.7

Note: b.d. = below detection limits, LOI = loss on ignition, Mg# = 100*molar MgO/(MgO + FeO^{tot}), $Eu/Eu^* = Eu_N / \sqrt{(Sm_N \times Gd_N)}$.

Table 2
Representative chemical compositions of the mylonitic syenite and alteration in Yangyang area.

Alteration type	Mylonitic syenite						Ca (–Na)	Ca							Ca–K				K			Phyllic
Sample	Y34	YY1006-3	YY1204-3	YY1204-5	YY1205-6	YY2010-7-9	YY2010-7-14	Y42	Y49	YY1003-7	YY1003-16	YY1003-18	YY2010-7-7A	YY2010-7-12	Y47	Y50	YY1003-10	YY2010-7-7B	YY1006-13	YY1203-10	YY1203-11	YY1004-1
Major elements (wt.%)																						
SiO_2	60.39	68.88	60.48	61.65	57.73	63.15	69.76	55.05	55.02	40.95	42.31	46.63	45.29	40.06	41.81	50.19	53.89	46.88	47.46	46.15	47.81	53.94
Al_2O_3	14.53	10.82	15.23	14.30	14.40	13.07	9.02	13.74	6.89	10.59	7.00	3.24	7.38	5.47	13.55	15.62	12.84	6.52	18.54	18.69	18.82	14.38
$Fe_2O_3^{tot}$	9.62	5.87	7.34	4.37	8.25	7.33	4.37	11.34	8.28	14.41	9.01	9.84	15.90	18.29	16.10	6.61	6.71	19.88	9.44	14.23	11.00	6.40
MnO	0.14	0.08	0.13	0.24	0.27	0.21	0.21	0.18	0.52	0.34	0.23	0.35	0.43	0.43	0.24	0.21	0.21	0.40	0.18	0.19	0.14	0.14
MgO	1.10	0.96	1.27	1.86	1.75	1.49	4.52	2.75	8.91	8.27	8.69	10.72	11.97	10.40	5.05	5.79	8.14	10.67	3.07	2.46	2.59	2.52
CaO	1.86	1.92	2.49	4.52	2.91	2.32	5.59	7.45	14.94	13.75	15.37	19.64	12.18	16.06	9.05	7.89	7.87	8.77	7.47	4.82	5.62	4.05
Na_2O	3.16	1.82	4.69	3.93	4.39	2.93	4.36	3.34	1.52	1.49	0.68	0.49	0.85	0.80	3.91	4.44	3.78	0.94	4.05	4.45	4.80	2.54
K_2O	6.52	5.32	3.71	5.66	4.07	5.37	0.47	3.65	3.01	1.82	3.31	1.13	1.14	0.96	2.75	3.06	2.64	1.61	3.11	2.79	2.88	4.58
TiO_2	1.11	0.37	1.00	1.24	1.03	0.93	0.24	0.41	0.33	3.06	10.26	5.73	1.08	0.76	3.29	2.64	0.32	0.11	2.32	2.25	2.26	0.74
P_2O_5	0.25	0.02	0.21	0.46	0.22	0.25	0.01	0.02	0.40	1.79	0.02	0.05	0.37	2.79	2.74	2.13	0.06	0.03	1.17	1.09	1.06	0.36
LOI	0.69	2.39	0.94	1.47	3.71	1.80	1.76	1.69	0.85	3.11	2.05	1.06	2.36	4.18	1.37	1.27	3.69	3.02	2.82	1.49	2.62	9.36
Total	99.38	98.45	97.50	99.70	98.73	98.85	100.30	99.62	100.70	99.57	98.92	98.88	98.93	100.20	99.87	99.84	100.20	98.83	99.62	98.61	99.59	99.00
$Na_2O + K_2O$	9.68	7.14	8.40	9.59	8.46	8.30	4.83	6.99	4.53	3.31	3.99	1.62	1.99	1.76	6.66	7.50	6.42	2.55	7.16	7.24	7.68	7.12
Mg#	18.5	24.5	25.5	45.7	29.6	28.7	67.2	32.5	68.1	53.2	65.6	68.3	59.9	53.0	38.3	63.4	70.6	51.5	39.2	25.5	31.8	43.8
Trace and rare earth elements (ppm)																						
Sc	6	3	7	7	5	4	2	8	2	32	21	19	27	9	18	23	7	1	15	12	12	12
Be	9	4	11	9	10	7	6	6	13	8	20	27	22	11	7	3	7	14	4	4	5	4
V	6	10	15	25	14	16	5	83	42	214	72	71	75	84	145	39	26	16	139	186	117	97
Cr	b.d.	b.d.	b.d.	b.d.	b.d.	b.d.	11	b.d.	b.d.	25	b.d.	18	9	12	b.d.	b.d.	6	b.d.	14	b.d.	b.d.	70
Co	2	2	3	4	2	2	13	11	19	19	10	11	34	75	18	14	18	110	11	10	7	11
Ni	3	b.d.	b.d.	b.d.	b.d.	b.d.	5	7	6	9	4	9	20	47	3	5	6	24	13	b.d.	b.d.	b.d.
Cu	3	b.d.	b.d.	b.d.	b.d.	b.d.	4	b.d.	3	6	3	6	23	207	b.d.	b.d.	2	172	7	b.d.	b.d.	b.d.
Zn	64	60	120	160	180	110	58	83	245	166	121	126	261	229	161	388	170	208	146	180	110	100
Ga	32	28	34	33	38	37	28	32	20	27	31	16	30	19	23	24	25	17	25	25	25	22
Ge	3.1	2.0	3.0	3.0	3.0	2.8	2.1	2.4	2.0	3.3	9.7	5.5	4.1	4.0	2.3	1.9	2.1	2.4	1.7	2.0	2.0	2.0

(continued on next page)

Table 2 (*continued*)

Alteration type	Mylonitic syenite						Ca (–Na)	Ca							Ca–K				K			Phyllic
Sample	Y34	YY1006-3	YY1204-3	YY1204-5	YY1205-6	YY2010-7-9	YY2010-7-14	Y42	Y49	YY1003-7	YY1003-16	YY1003-18	YY2010-7-7A	YY2010-7-12	Y47	Y50	YY1003-10	YY2010-7-7B	YY1006-13	YY1203-10	YY1203-11	YY1004-1
As	5	b.d.	b.d.	b.d.	b.d.	b.d.	b.d.	b.d.	b.d.	8	b.d.	b.d.	3	20	11	12	b.d.	b.d.	4	b.d.	b.d.	b.d.
Rb	180	105	75	116	119	170	10	79	62	106	258	100	32	22	127	139	117	76	183	136	170	165
Sr	189	190	357	216	387	182	70	315	122	151	74	37	89	64	332	332	406	36	743	557	491	354
Y	86.2	120.0	88.0	115.0	99.0	101.0	83.6	64.7	62.3	83.6	795.0	464.0	91.7	174.0	54.0	106.0	38.5	73.2	27.2	33.0	87.0	38.0
Zr	1550	1647	1471	700	1481	1040	1340	2910	1300	237	633	468	334	1260	271	494	992	549	210	180	194	282
Nb	194.0	154.0	202.0	174.0	256.0	210.0	215.0	186.0	90.3	119.0	909.0	528.0	117.0	109.0	62.0	166.0	67.5	120.0	34.4	24.0	34.0	57
Mo	b.d.	b.d.	b.d.	5	b.d.	b.d.	7	b.d.	b.d.	5	16	9	b.d.	b.d.	9	11	13	9	b.d.	b.d.	b.d.	b.d.
Ag	b.d.	b.d.	b.d.	4.4	b.d.	b.d.	b.d.	b.d.	b.d.	b.d.	b.d.	b.d.	b.d.	b.d.	b.d.	b.d.	b.d.	0.4	b.d.	1.1	0.9	1.2
In	b.d.	b.d.	b.d.	b.d.	b.d.	b.d.	b.d.	b.d.	0.1	0.1	0.2	0.2	0.2	0.2	b.d.	b.d.	b.d.	0.2	b.d.	b.d.	b.d.	b.d.
Sn	11	14	9	12	11	14	6	14	6	23	100	60	27	45	11	13	7	22	12	7	8	5
Sb	b.d.	0.5	b.d.	b.d.	b.d.	0.8	b.d.	b.d.	b.d.	b.d.	1.6	0.8	b.d.	b.d.	b.d.	b.d.	b.d.	b.d.	0.5	b.d.	b.d.	12.4
Cs	0.9	1.4	1.2	0.7	1.5	2.6	0.3	0.2	0.1	3.5	6.3	3.3	1.3	0.6	4.0	2.4	3.7	1.6	5.8	3.7	3.7	8.6
Ba	808	274	767	793	794	401	18	788	279	117	184	65	69	31	334	558	501	262	759	728	294	950
La	190.0	247.0	166.0	200.0	188.0	148.0	46.2	68.8	92.5	207.0	945.0	477.0	212.0	446.0	244.0	262.0	46.3	100.0	66.6	168.0	172.0	61.8
Ce	391.0	470.0	329.0	431.0	365.0	315.0	104.0	147.0	174.0	392.0	2250.0	1190.0	407.0	749.0	434.0	484.0	90.4	186.0	107.0	248.0	283.0	127.0
Pr	41.9	52.1	36.6	47.2	37.5	34.2	13.1	16.3	18.2	42.9	258.0	145.0	40.9	71.4	33.0	50.8	10.8	19.8	12.8	21.1	25.6	13.3
Nd	156.0	186.0	127.0	170.0	131.0	129.0	58.0	65.8	71.5	159.0	936.0	572.0	141.0	253.0	122.0	195.0	43.6	75.6	55.4	66.9	83.8	44.7
Sm	25.40	34.00	23.70	31.20	23.40	25.70	15.90	15.50	14.30	28.90	189.00	118.00	24.20	44.10	20.90	34.70	8.94	17.70	11.00	10.90	14.40	7.90
Eu	4.75	3.42	5.20	5.82	5.04	4.07	2.12	1.90	1.85	5.70	30.10	18.40	3.44	5.88	7.12	9.18	1.34	2.32	3.58	3.40	4.67	1.90
Gd	20.90	28.30	18.70	23.80	18.60	22.10	15.50	14.50	13.10	23.10	159.00	103.00	20.00	39.50	18.20	29.30	8.18	15.70	9.44	8.60	12.30	6.30
Tb	3.34	4.60	3.00	3.90	3.30	3.53	2.82	2.55	2.23	3.57	27.00	17.40	3.06	5.78	2.37	4.19	1.37	2.52	1.30	1.20	2.20	1.00
Dy	18.30	24.90	16.90	21.70	19.60	20.50	17.00	15.30	12.30	19.20	153.00	97.70	17.50	32.70	11.70	22.00	7.79	14.30	6.47	6.50	13.30	6.30
Ho	3.37	4.60	3.30	4.10	3.90	3.83	3.28	3.08	2.30	3.62	29.80	19.00	3.40	6.31	2.04	4.07	1.59	2.62	1.16	1.10	2.80	1.30
Er	9.49	12.40	9.20	11.30	10.80	11.10	9.39	9.23	6.74	9.32	77.60	50.50	9.75	17.60	5.41	10.70	4.45	7.46	2.88	3.10	8.00	4.00
Tm	1.40	1.73	1.36	1.61	1.56	1.60	1.44	1.48	1.10	1.27	11.00	6.86	1.47	2.44	0.77	1.49	0.72	1.17	0.38	0.42	1.15	0.62
Yb	8.52	10.40	8.80	10.00	9.80	10.40	10.00	9.68	8.00	7.64	68.00	41.30	9.84	14.40	4.66	8.80	4.78	8.34	2.34	2.50	7.10	4.20
Lu	1.200	1.590	1.400	1.570	1.510	1.550	1.640	1.440	1.380	1.090	9.690	5.850	1.640	2.080	0.670	1.250	0.800	1.390	0.334	0.360	1.020	0.690
Hf	30.6	34.9	27.5	17.1	32.2	24.4	31.6	73.4	29.7	5.2	13.0	10.5	8.3	26.4	6.4	10.6	23.8	16.4	4.3	4.4	4.2	7.2
Ta	10.50	12.30	11.30	9.60	16.90	12.60	14.10	24.50	11.40	4.99	44.30	221.00	8.73	9.10	3.63	7.44	7.23	10.10	2.67	1.30	2.10	6.40
W	1.5	b.d.	b.d.	b.d.	2.0	1.2	3.9	b.d.	b.d.	0.6	3.5	2.4	1.1	21.2	0.9	b.d.	b.d.	1.5	b.d.	b.d.	1.0	2
Tl	0.3	0.4	0.3	0.7	0.4	0.4	0.1	0.3	0.3	0.4	0.5	0.3	0.2	0.1	0.3	0.5	0.6	0.2	1.0	0.7	0.4	0.7
Pb	12.00	17	18.00	15.00	14.00	14.00	b.d.	20.00	9	12	12	9	b.d.	7	10	10	b.d.	b.d.	17	22	11	16
Bi	b.d.	b.d.	b.d.	b.d.	b.d.	0.1	b.d.	0.1	b.d.	0.2	0.4	0.6	0.3	0.4	0.1	0.1	b.d.	0.1	0.1	b.d.	b.d.	b.d.
Th	31.1	35.1	26.5	16.7	32.6	25.0	33.6	21.4	6.1	12.6	165.0	83.4	15.3	42.5	4.7	10.2	18.1	19.5	3.9	4.1	4.3	7.8
U	6.38	3.70	4.80	3.40	5.80	5.66	8.27	8.44	2.08	3.28	21.10	16.70	2.59	7.07	3.94	2.97	3.47	7.22	1.42	1.00	2.10	2.70
$\sum$ REE	875.6	1081.0	750.2	963.2	819.0	730.6	300.4	372.6	419.5	904.3	5143.2	2862.0	895.2	1690.2	906.8	1117.5	231.1	454.9	280.7	542.1	631.3	281.0
Eu/Eu^*	0.63	0.34	0.76	0.65	0.74	0.52	0.41	0.39	0.41	0.67	0.53	0.51	0.48	0.43	1.12	0.88	0.48	0.43	1.07	1.07	1.07	0.82
La_N/Yb_N	16.0	17.0	13.5	14.3	13.8	10.2	3.3	5.1	8.3	19.4	10.0	8.3	15.5	22.2	37.6	21.4	6.9	8.6	20.4	48.2	17.4	10.6

Note: b.d. = below detection limits, LOI = loss on ignition, Mg# = 100*molar MgO/(MgO + FeO^{tot}), $Eu/Eu^* = Eu_N / \sqrt{(Sm_N \times Gd_N)}$.

Table 3
SHRIMP U–Pb zircon age data from undeformed syenite in the Yangyang area, South Korea.

Sample: YY110715-1													Age (Ma)				
Spot	$^{206}Pb_c$	U	Th	U/Th	$^{207}Pb/^{206}Pb$	±%	(1)		Err.	(2)		Err.	(1)		(2)		(%)
	(%)	(ppm)	(ppm)	Ratio			$^{207}Pb^*/^{206}Pb^*$	±%	Corr	$^{207}Pb^*/^{206}Pb^*$	±%	Corr	$^{206}Pb/^{238}U$		$^{206}Pb/^{238}U$		Discordant
1	0.00	266.70	203.40	0.77	0.050	2.5	0.053	4.9	0.3	0.050	3.8	0.4	234	±3	233	±4	+33
2	0.28	255.80	240.80	0.94	0.053	2.5	0.053	7.3	0.3	0.051	5.9	0.4	232	±5	231	±6	+32
3	0.00	272.10	171.50	0.63	0.049	2.5	0.050	5.3	0.2	0.051	3.0	0.4	233	±3	233	±3	−32
4	0.00	225.30	138.30	0.61	0.051	2.9	0.048	9.9	0.2	0.050	3.7	0.4	230	±4	231	±5	−191
5	0.53	244.30	143.70	0.59	0.055	2.5	0.054	5.9	0.3	0.051	3.2	0.4	231	±4	230	±4	+41
6	0.00	142.30	140.00	0.99	0.051	3.4	0.051	10.0	0.2	0.045	9.4	0.4	238	±4	237	±4	−3
7	0.33	264.90	188.50	0.71	0.053	2.5	0.054	5.7	0.2	0.053	3.4	0.4	229	±3	229	±3	+41
8	0.00	257.10	175.30	0.68	0.050	2.6	0.051	6.4	0.3	0.049	3.7	0.4	236	±4	236	±5	−6
9	0.02	269.90	256.10	0.95	0.051	2.4	0.053	5.1	0.2	0.043	6.6	0.4	229	±3	227	±3	+26
10	0.00	215.50	131.30	0.61	0.050	2.8	0.050	8.6	0.2	0.045	3.7	0.4	238	±3	236	±4	−30

Errors are 1-sigma; Pb_c and Pb^* indicate the common and radiogenic portions, respectively.
Error in standard calibration was 0.25% (not included in above errors but required when comparing data from different mounts).
(1) Common Pb corrected using measured ^{204}Pb.
(2) Common Pb corrected by assuming $^{206}Pb/^{238}U$–$^{208}Pb/^{232}Th$ age-concordance.

Table 4
Representative chemical compositions of the biotite in Yangyang area, South Korea.

Rock type	Syenite/cataclastic syenite							Alterations											Magnetite ore						Magnetite–pyrite ore		
Sample	YYN1409-102B				YY2010-7-21-2			YY1003-18		903-2		Domok 2	B-2	28	Y37	Y47	18	904-2	16		402		905-2		410-2		
Analysis	yy1545	yy1546	yy1547	yy1548	yy1056	yy1057	yy1119	yy754	yy1149	yy044	yy048	yy506	yy469	yy249	yy918	yy1531	yy447	yy402	yy095	yy096	yy025	yy300	yy345	yy352	yy108	yy106	yy480
SiO_2	36.69	36.48	36.84	36.72	36.02	36.32	36.30	40.27	40.25	38.36	38.09	38.81	38.52	37.99	38.39	39.12	37.90	39.18	37.48	37.16	39.58	39.04	39.52	40.58	41.32	40.97	40.92
TiO_2	2.78	2.71	2.72	2.76	1.88	1.93	1.58	0.43	0.68	1.05	1.08	0.68	0.88	1.18	0.92	0.72	1.15	0.61	1.96	1.99	1.00	0.73	0.73	0.56	0.43	0.37	0.53
Al_2O_3	13.75	13.82	13.61	13.62	15.98	16.05	15.46	12.28	11.79	12.72	13.41	12.66	13.44	13.37	13.38	12.07	13.74	12.20	14.04	14.16	12.80	12.65	12.34	11.92	10.86	11.07	11.17
FeO	19.80	20.13	20.27	19.92	19.09	19.35	21.87	12.55	13.79	15.04	14.98	13.98	15.21	15.58	14.20	13.41	17.58	14.67	18.22	18.53	12.17	11.70	10.78	10.36	9.16	9.33	9.16
MnO	0.34	b.d.	0.37	0.35	b.d.	0.30	0.29	0.28	b.d.	0.48	0.39	0.38	0.29	b.d.	0.35	0.58	b.d.	0.29	b.d.	b.d.	b.d.	0.33	b.d.	b.d.	b.d.	b.d.	b.d.
MgO	11.59	11.32	11.55	11.64	11.57	11.81	10.73	18.83	18.10	16.57	16.16	16.93	16.20	15.77	16.72	17.76	13.54	17.06	13.79	13.58	18.79	19.02	20.02	20.52	22.10	21.71	21.41
Na_2O	b.d.	b.d.	b.d.	b.d.	b.d.	0.31	b.d.	b.d.	b.d.	b.d.	0.31	b.d.	0.29	0.34	b.d.	b.d.	b.d.	b.d.	0.44	0.42	b.d.	b.d.	b.d.	0.30	b.d.	b.d.	0.32
K_2O	10.53	10.53	10.58	10.57	10.30	10.19	10.24	10.73	11.26	10.68	10.47	11.11	10.54	10.17	10.80	10.88	10.89	11.03	9.62	9.69	10.05	10.61	11.12	10.94	10.29	10.17	10.83
Total	95.48	94.99	95.94	95.58	94.84	96.26	96.47	95.37	95.87	94.90	94.89	94.55	95.37	94.40	94.76	94.54	94.80	95.04	95.55	95.53	94.39	94.08	94.51	95.18	94.16	93.94	94.34
Number of cations on the basis of 22 (O)																											
Si	5.66	5.66	5.67	5.66	5.55	5.52	5.57	5.96	5.98	5.81	5.76	5.87	5.79	5.77	5.79	5.90	5.80	5.91	5.68	5.65	5.89	5.85	5.88	5.97	6.07	6.05	6.03
Al^{IV}	2.34	2.34	2.34	2.34	2.46	2.48	2.43	2.04	2.02	2.19	2.24	2.13	2.21	2.23	2.21	2.10	2.20	2.09	2.32	2.35	2.11	2.15	2.12	2.03	1.88	1.92	1.94
Al^{VI}	0.15	0.18	0.13	0.13	0.44	0.39	0.36	0.11	0.04	0.08	0.15	0.13	0.18	0.17	0.17	0.05	0.28	0.08	0.19	0.19	0.13	0.09	0.04	0.03	0.00	0.00	0.00
Ti	0.32	0.32	0.32	0.32	0.22	0.22	0.18	0.05	0.08	0.12	0.12	0.08	0.10	0.14	0.10	0.08	0.13	0.07	0.22	0.23	0.11	0.08	0.08	0.06	0.05	0.04	0.06
Fe^{2+}	2.55	2.61	2.61	2.57	2.46	2.46	2.81	1.55	1.71	1.91	1.90	1.77	1.91	1.98	1.79	1.69	2.25	1.85	2.31	2.36	1.51	1.47	1.34	1.27	1.13	1.15	1.13
Mn	0.04	0.00	0.05	0.05	0.00	0.04	0.04	0.04	0.00	0.06	0.05	0.05	0.04	0.00	0.05	0.07	0.00	0.04	0.00	0.00	0.00	0.04	0.00	0.00	0.00	0.00	0.00
Mg	2.66	2.62	2.65	2.68	2.66	2.68	2.45	4.16	4.01	3.74	3.64	3.82	3.63	3.57	3.76	4.00	3.09	3.84	3.12	3.08	4.17	4.25	4.44	4.50	4.84	4.78	4.71
Na	0.00	0.00	0.00	0.00	0.00	0.09	0.00	0.00	0.00	0.00	0.09	0.00	0.09	0.10	0.00	0.00	0.00	0.00	0.13	0.12	0.00	0.00	0.00	0.09	0.00	0.00	0.09
K	2.07	2.08	2.08	2.08	2.02	1.98	2.00	2.03	2.13	2.06	2.02	2.15	2.02	1.97	2.08	2.10	2.13	2.12	1.86	1.88	1.91	2.03	2.11	2.05	1.93	1.92	2.04
Cations	15.81	15.80	15.82	15.82	15.80	15.85	15.85	15.93	15.98	15.97	15.97	15.99	15.97	15.93	15.95	15.99	15.88	16.00	15.83	15.85	15.83	15.96	16.01	16.00	15.90	15.95	16.00
Mg#	0.51	0.50	0.50	0.51	0.52	0.52	0.47	0.73	0.70	0.66	0.66	0.68	0.66	0.64	0.68	0.70	0.58	0.67	0.57	0.57	0.73	0.74	0.77	0.78	0.81	0.81	0.81

Note: b.d. = below detection limits, Mg# = $Mg/(Mg + Fe^{2+})$.

Table 5
Representative results of LA-ICP-MS analyses of trace elements within sphene in the Yangyang area, South Korea.

Rock type	Cataclastic syenite									Alteration						Magnetite ore		
Sample	YY1001-1			YY2010-7-13			YY2010-7-22			Y47			Y50			Y37		
Trace and rare earth elements (ppm)					6*	7*					1*	2*						
Mg	309.9	258.2	198.7	1342.4	544.4	906.6	630.2	564.5	212.4	621.5	711.7	859.7	1901.3	3025.1	6789.6	801.2	738.4	615.6
P	312.2	311.3	313.9	89.3	276.4	55.4	249.3	407.0	267.9	143.2	172.3	183.2	73.0	222.7	212.7	105.5	96.2	111.2
V	669.8	670.5	662.3	738.6	710.3	664.1	703.7	644.0	677.4	220.3	231.5	242.4	164.2	197.7	215.6	332.7	406.6	348.2
Mn	848.7	852.9	898.4	790.3	1167.6	675.2	815.0	816.7	770.3	1629.5	1599.2	1564.6	1130.0	1851.2	1927.5	615.9	645.7	614.0
Sr	80.8	73.0	70.3	38.1	63.7	32.8	65.4	82.3	63.8	35.7	37.5	32.1	23.2	28.1	25.6	23.5	27.1	17.8
Y	1396.4	1309.3	1489.3	2553.5	3697.6	1625.0	1163.9	1175.2	1360.0	392.5	602.8	554.3	1131.7	2142.5	1746.9	945.1	742.7	803.1
Zr	579.8	523.7	572.5	306.7	839.9	166.9	474.5	511.9	459.0	540.8	760.9	547.3	676.9	672.0	654.9	1606.9	1574.1	1233.3
La	2429.8	2436.5	2453.0	1207.0	3900.1	247.2	1751.3	2756.3	2486.1	800.8	1323.5	1592.7	1292.8	3810.0	3279.0	1628.3	2251.9	1908.1
Ce	7525.9	6291.8	7839.4	3863.1	10979.8	1163.5	5255.3	7443.7	6475.8	1901.9	2824.3	3405.2	3072.2	8881.9	7618.8	3992.8	4851.9	4420.3
Pr	938.9	729.8	996.7	561.7	1401.9	216.3	632.5	853.4	776.8	168.2	241.6	278.1	357.7	972.5	853.1	459.4	516.7	481.1
Nd	3671.5	2744.4	3896.3	2571.4	5618.4	1140.3	2411.9	3186.2	3029.1	729.7	983.7	1081.0	1401.8	3627.1	3226.0	1694.8	1794.7	1701.8
Sm	630.5	459.7	677.2	648.7	1159.3	329.0	419.8	513.9	535.4	157.1	205.3	206.5	290.7	652.8	573.1	293.5	268.7	265.9
Eu	136.8	118.9	145.9	104.6	148.8	96.3	97.4	113.7	137.2	59.6	78.0	73.6	93.4	156.0	137.7	59.1	53.4	54.4
Gd	417.5	317.7	448.2	529.4	851.3	285.8	291.1	340.6	376.2	120.5	170.9	165.7	239.5	504.5	434.9	215.1	178.2	187.6
Tb	58.5	46.3	62.8	89.5	138.1	48.9	42.7	47.9	53.6	16.3	24.6	22.8	37.7	77.7	65.3	32.1	25.4	27.3
Dy	316.0	262.2	343.3	530.3	790.1	296.6	243.0	260.8	297.5	85.1	133.5	122.5	218.4	444.7	367.7	183.2	140.6	152.3
Ho	57.0	50.0	61.5	100.7	148.2	58.6	44.9	47.2	54.4	15.4	24.4	22.0	41.6	83.9	68.2	35.9	26.9	29.6
Er	141.5	133.1	153.4	266.9	388.5	165.1	118.9	119.1	139.3	38.9	60.2	54.2	111.4	218.6	176.8	93.5	71.5	79.6
Tm	19.0	19.2	20.5	37.2	54.4	25.0	17.0	16.1	18.9	5.2	7.9	7.2	15.8	29.2	23.5	12.6	9.8	10.8
Yb	126.5	137.5	137.8	247.3	350.9	182.4	120.5	107.2	127.8	35.0	52.2	47.5	109.9	187.1	151.1	81.8	63.5	71.0
Th	769.3	810.4	807.6	239.7	643.8	66.7	552.1	793.7	540.4	30.4	44.6	50.7	84.5	362.5	266.6	98.7	40.1	125.2
U	138.2	175.7	141.0	159.3	100.5	193.5	112.0	108.4	142.3	42.8	50.0	45.9	27.7	83.4	63.7	25.9	20.3	28.7
REE total	16469	13747	17236	10758	25930	4255	11446	15806	14508	4134	6130	7079	7283	19646	16975	8782	10253	9390
Eu/Eu^*	0.82	0.95	0.81	0.55	0.46	0.96	0.85	0.83	0.93	1.32	1.27	1.22	1.08	0.83	0.84	0.72	0.75	0.74
La_N/Yb_N	13.8	12.7	12.8	3.5	8.0	1.0	10.4	18.4	14.0	16.4	18.2	24.0	8.4	14.6	15.6	14.3	25.4	19.3

Note: $Eu/Eu^* = Eu_N / \sqrt{(Sm_N \times Gd_N)}$; 1*–2* and 6*–7* show the Figs. 12A and 13A, respectively.

Table 6
Representative results of LA-ICP-MS analyses of trace elements within apatite in the Yangyang area, South Korea.

Rock type	Magnetite ore																Magnetite–pyrite ore							
Sample	B1								Y37								Y35							
																					3*	4*	5*	
CaO (wt.%)	54.7	54.7	55.2	54.9	54.7	55.2	55.4	55.5	54.4	54.8	54.6	54.7	55.1	54.9	54.4	56.0	54.7	55.5	54.3	55.5	53.9	54.5	55.4	56.0
Trace and rare earth elements (ppm)																								
Mg	605.7	659.6	176.7	388.7	45.1	273.8	208.1	16.3	305.9	144.4	287.8	38.1	60.8	357.2	296.8	17.2	146.1	1444.6	908.7	123.5	667.1	292.0	12.3	15.1
Al	396.7	491.1	104.9	247.6	23.9	164.5	132.3	1.3	159.4	73.4	238.5	21.3	24.3	192.3	213.1	2.9	0.0	502.7	120.3	0.9	210.4	11.4	0.0	0.1
Si	3241.0	3739.1	2681.9	2718.8	2775.6	2274.5	2275.7	1411.6	6895.9	4011.6	5051.0	6748.4	5666.7	4312.4	3830.9	2314.7	4249.8	6416.1	8643.9	3127.9	8415.7	4775.4	2433.7	2108.2
S	506.5	616.2	540.3	549.0	631.5	541.4	536.8	472.8	1561.7	1281.3	1660.6	2204.8	1545.0	1365.9	1215.6	1011.2	1010.7	734.2	1284.4	1111.8	1365.0	855.2	976.1	1090.2
Mn	232.7	249.2	213.4	205.9	207.5	234.7	219.7	221.1	241.4	249.5	258.5	336.0	334.2	243.6	260.1	218.1	357.0	378.3	251.2	203.5	277.4	199.2	180.2	179.5
Sr	500.1	508.0	478.0	506.7	561.7	489.8	484.2	460.9	335.0	316.5	323.9	286.1	264.2	322.8	281.1	306.8	349.2	658.7	366.4	329.7	330.6	327.0	343.9	328.0
Y	1257.3	1245.6	1187.1	936.7	1230.2	901.8	959.5	375.7	400.5	280.5	319.2	409.6	324.0	159.1	90.7	56.2	773.8	625.7	850.0	482.8	1273.9	821.2	206.6	209.5
La	1054.5	1511.3	977.0	776.7	1545.3	453.3	553.3	150.6	3307.3	1970.6	2742.8	4084.7	3334.2	1462.8	952.5	366.6	3228.7	1379.8	3690.3	1200.2	4111.6	2462.9	510.4	690.7
Ce	2371.5	3119.6	2141.2	1697.2	3197.9	1135.6	1317.7	396.5	5164.5	3124.3	4085.8	6106.5	4506.4	2151.0	1376.3	577.9	4782.5	2209.2	5740.4	2256.4	6760.8	3959.1	906.2	1212.6
Nd	1089.6	1357.2	1074.5	849.9	1403.4	633.9	688.6	256.1	1235.1	813.5	989.7	1373.1	1073.8	474.4	311.9	151.4	1440.5	759.3	1707.7	785.4	2232.2	1374.2	350.0	398.9
Sm	209.2	253.1	215.4	168.6	249.7	131.9	144.7	55.6	124.5	93.7	113.0	149.7	121.2	50.1	30.2	16.7	217.8	131.6	256.4	124.4	351.4	217.6	56.5	60.7
Eu	20.6	24.8	20.9	16.1	24.8	13.4	13.9	5.3	25.3	14.4	18.1	24.1	21.0	9.8	6.2	2.8	20.7	14.1	24.5	12.5	33.7	20.9	5.4	5.8
Gd	219.4	248.0	227.1	177.0	242.6	148.7	164.0	65.9	98.1	76.3	89.4	115.1	95.0	38.7	23.8	14.1	188.2	137.4	216.7	111.9	306.1	192.4	49.7	53.2
Dy	197.8	206.8	193.5	150.8	203.1	138.8	149.6	58.2	54.8	43.0	52.0	64.7	54.0	22.7	12.5	7.8	133.0	108.9	150.0	82.1	223.5	140.8	35.5	36.3
Yb	96.2	89.4	83.3	65.3	86.2	71.2	70.0	25.8	29.6	18.3	21.3	27.5	21.6	11.1	6.2	3.6	45.7	32.8	49.6	29.1	80.4	50.6	11.2	11.9
Lu	13.5	12.4	11.4	8.9	11.6	10.2	9.6	3.6	5.4	3.1	3.4	4.6	3.3	2.0	1.2	0.6	5.8	3.8	6.3	3.8	10.2	6.3	1.5	1.5
Th	95.3	84.2	58.8	61.4	93.6	26.9	33.4	1.6	313.2	131.7	138.3	246.6	111.2	54.2	28.5	8.3	253.3	120.0	274.8	95.3	622.2	208.8	22.3	31.1
U	26.7	32.4	23.2	19.0	36.6	12.0	12.7	1.7	41.1	9.7	11.1	22.6	9.3	6.3	3.5	0.8	12.6	7.7	13.7	7.1	37.9	15.0	2.0	2.5
REE total	5272	6823	4944	3910	6965	2737	3111	1018	10045	6157	8115	11950	9230	4222	2721	1142	10063	4777	11842	4606	14110	8425	1926	2472
Eu/Eu*	0.29	0.30	0.29	0.29	0.31	0.29	0.28	0.27	0.70	0.52	0.55	0.56	0.60	0.68	0.71	0.56	0.31	0.32	0.32	0.32	0.31	0.31	0.31	0.31
La_N/Yb_N	7.9	12.1	8.4	8.5	12.9	4.6	5.7	4.2	80.0	77.3	92.5	106.6	110.7	94.8	109.4	73.5	50.6	30.2	53.4	29.6	36.7	34.9	32.7	41.8
Mineral assemblages	Magnetite > amphibole + apatite + biotite + sphene (high-grade magnetite ore with Ca, Ca–K alteration)								Biotite + amphibole + magnetite + sphene + apatite (low-grade magnetite ore with Ca–K, K alteration)								Magnetite + pyrite + chalcopyrite + apatite + amphibole + muscovite + biotite + chlorite (magnetite–pyrite ore with K, phyllic alterations)							

Note: High-grade magnetite ore (up to 60 wt.% $Fe_2O_3^{tot}$); $Eu/Eu^* = Eu_N / \sqrt{(Sm_N * Gd_N)}$; 3*–5* shows Fig. 12D.

Microsoft Excel™ spreadsheet, following Longerich et al. (1996). Detection limits for the analyzed elements were calculated using the relationship described by Longerich et al. (1996) and Sylvester and Eggins (1997). The analytical technique for sphene and apatite used in this study is similar to the procedure described by Allen and Campbell (2012), except that Mud Tank zircon (Black and Gulson, 1987) was used as a primary standard. Raw count rates for ^{206}Pb, ^{207}Pb, ^{208}Pb, ^{232}Th, and ^{238}U were recorded in time-resolved mode by peak hopping. Data were acquired for 25 s with the laser off and 40 s with the laser on, giving approximately 100 mass sweeps for a penetration depth of ~20 μm. Standards were analyzed before and after analysis of 10 unknown sphene or apatite points in a 16-analysis rotation, as follows: NIST 610 standard silicate glass, Mud Tank zircon standard, Mud Tank apatite standard, unknown sphene or apatite, NIST 610 standard silicate glass, Mud Tank zircon standard, and Mud Tank apatite standard. Trace element concentrations of sphene and apatite are listed in Tables 5 and 6, respectively.

4. Geochemistry and age of the Triassic intrusion

4.1. Major and trace element geochemistry of the Yangyang syenites and granites

The Yangyang syenites and cataclastic syenites have similar compositions to each other, with 52.4–61.7 wt.% SiO_2, 14.4–17.0 wt.% Al_2O_3, 5.8–8.6 wt.% $Fe_2O_3^{tot}$, 3.0–6.4 wt.% CaO, 3.1–4.4 wt.% Na_2O, 3.2–6.7 wt.% K_2O, 0.4–1.2 wt.% TiO_2, 0.3–0.6 wt.% P_2O_5, and a Mg# of 42.3–55.4. The mylonitic syenites are strongly altered and deformed. They have lost their magmatic compositions and are considered with alteration products in Section 4.1. The Yangyang granites contain about 63.5 wt.% SiO_2, 14.7–16.6 wt.% Al_2O_3, 5.3–5.7 wt.% $Fe_2O_3^{tot}$, 3.4–4.7 wt.% CaO, 3.3–3.6 wt.% Na_2O, 2.5–3.2 wt.% K_2O, 0.5–0.6 wt.% TiO_2, 0.2–0.4 wt.% P_2O_5, and have a Mg# of 35.6–48.8 (Table 1). On the total alkali ($Na_2O + K_2O$) vs. silica diagram (Cox et al., 1979), the syenites and cataclastic syenites plot in the alkaline field (syenite to syenodiorite), whereas the granites fall in the subalkaline granodiorite field (Fig. 7A). On the SiO_2 vs. K_2O (wt.%) binary diagram (Peccerillo and Taylor, 1976), the syenites and cataclastic syenites show shoshonitic affinities, with K_2O concentrations ranging from 7.4 to 10.1 wt.%; these syenites also have high Ba and Sr concentrations (1647–2753 and 533–1281 ppm, respectively). The granites have a high-K calc-alkaline signature, with $Na_2O + K_2O$ of 5.8–6.8 wt.%, and have Ba concentrations of 683–1087 ppm and Sr concentrations of 500–858 ppm (Table 1; Fig. 7B). On tectonic discrimination diagrams (after Harris et al., 1986; Pearce, 1996; Pearce et al., 1984), the syenites, cataclastic syenites, and granites plot in the post-collisional granite (post-COLG) fields of Rb/Zr vs. SiO_2 and Rb vs. Y + Nb diagrams, respectively (Fig. 7C, D). The syenites and cataclastic syenites have similar total REE concentrations to the granites (236–441 and 307–409 ppm, respectively; Table 1). The syenites and cataclastic syenites display similar LREE-enriched chondrite-normalized (Sun and McDonough, 1989) REE patterns; the granites display relatively more fractionated patterns, with La_N/Yb_N ratios of 37–46 compared with 12–29 for the syenites and cataclastic syenites (Fig. 8A, C, E). The Eu anomalies ($Eu/Eu^* = Eu_N /$

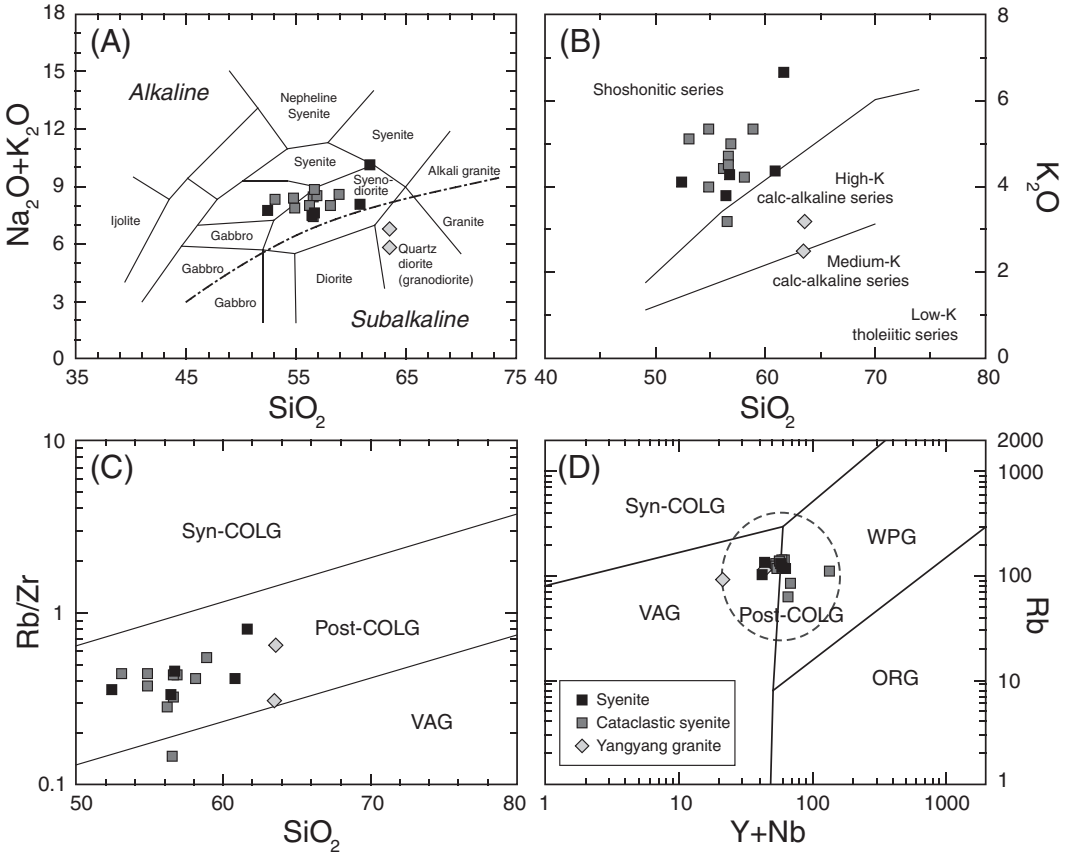

Fig. 7. Geochemistry and tectonic discrimination diagrams for Triassic post-collisional igneous rocks in the Yangyang area. (A) Total alkalis vs. silica (TAS) diagram for Triassic igneous rocks. The dashed line separates the fields for alkaline and subalkaline magmas (after Cox et al., 1979; Wilson, 1989). (B) Subdivision of subalkalic rocks based on the SiO_2 vs. K_2O diagram (after Peccerillo and Taylor, 1976). (C) SiO_2 (wt.%) vs. Rb/Zr diagram (Harris et al., 1986) for Triassic igneous rocks. (D) Y + Nb versus Rb (ppm) variation diagram for Triassic igneous rocks (Pearce, 1996; Pearce et al., 1984). Abbreviations: Syn-COLG—syn-collision granites; post-COLG—post-collision granites; VAG—volcanic arc granites; WPG—within-plate granite; ORG—ocean ridge granites.

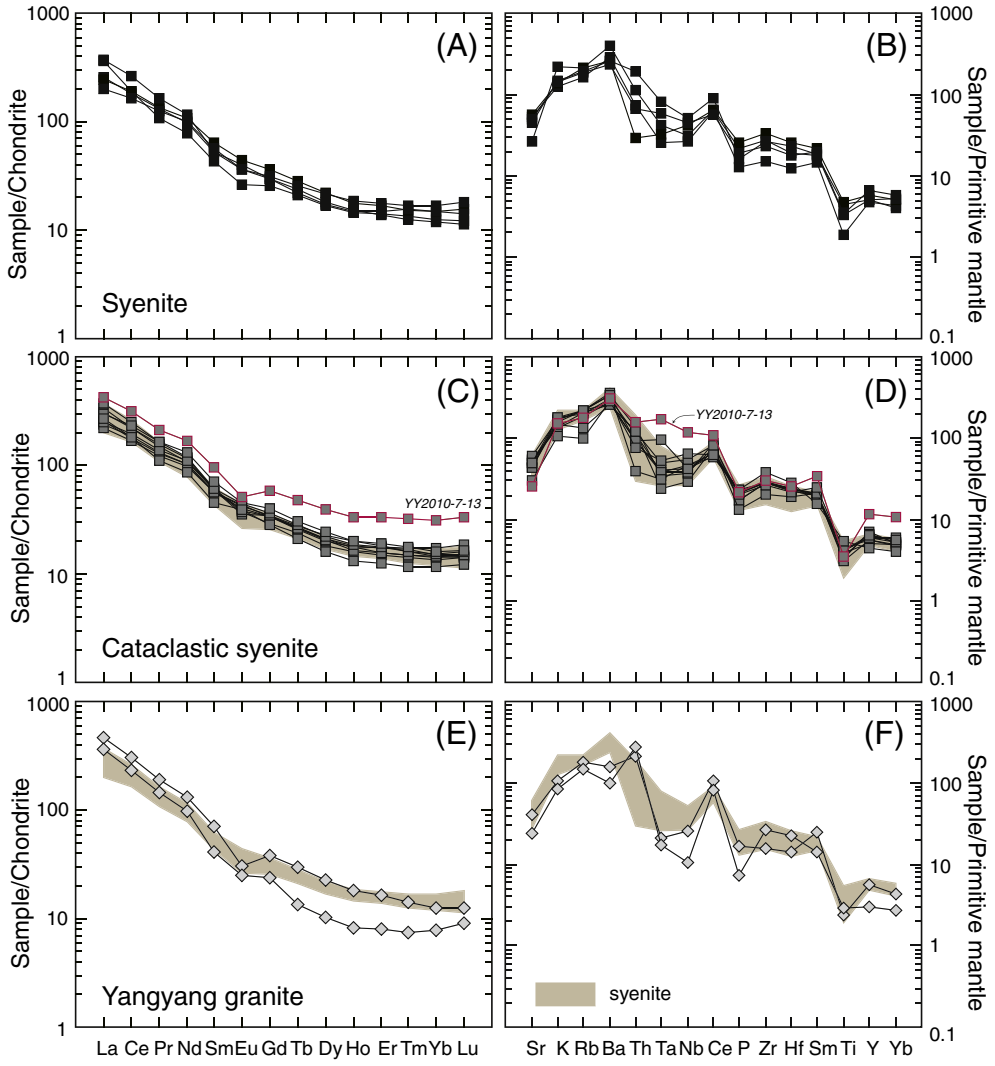

Fig. 8. Chondrite-normalized REE patterns and primitive-mantle-normalized trace element patterns of syenites. (A, B) Yangyang syenite. (C, D) Cataclastic syenite. (E, F) Yangyang granite. Syenite fields from A and B are shaded for comparison on C–F. The symbols are the same as in Fig. 7.

$\sqrt{[Sm_N \times Gd_N]}$) of the syenites and cataclastic syenites (0.8–1.1; except for sample YY2010-7-13 = 0.7) are less negative than those of the granites (0.6–0.8; Table 1; Fig. 8A, C, E). All rocks have distinctive negative high-field strength element (HFSE) anomalies (Nb, Ta, Ti) on primitive-mantle-normalized multi-element plots, indicating a subduction-related contribution to the magma (Fig. 8B, D, F). An exceptionally sphene-rich sample (YY2010-7-13) contains relatively high Nb (83.4 ppm), Ta (6.8 ppm), and heavy REE (HREE) concentrations (Fig. 8C, D).

4.2. SHRIMP U–Pb dating of zircon

Sample YY110715-1 is a medium- to coarse-grained syenite. The zircons in this sample vary in size from 100 to 150 μm and have aspect ratios of 1.2–1.8. CL images reveal that all the grains are concentrically zoned (Fig. 9A). The zircon morphologies are prismatic without overgrowth rims. U–Pb isotope analyses of 10 spots are plotted on a Tera–Wetherill concordia plot (Fig. 9B). The zircons have Th concentrations of 131–256 ppm and U concentrations of 142–272 ppm, with Th/U values of 0.61–0.99 (Table 3). The ten analyses give apparent $^{206}Pb/^{238}U$ ages of 229–238 Ma. The weighted mean age for all igneous zircons is 232.9 ± 1.1 Ma (n = 10, MSWD = 1.2). The zircons from the Yangyang syenite do not have older inherited cores and yield a single igneous age.

5. Geochemistry of the syenite alteration products and ores

5.1. Geochemistry and mineral chemistry of mylonitic syenites and alteration materials

The mylonitic syenites have slightly different major-element compositions to the undeformed syenites and show a compositional range as follows: SiO_2 (57.7–68.9 wt.%), Al_2O_3 (10.8–14.5 wt.%), Fe_2O_3 (4.4–9.6 wt.%), CaO (1.9–4.5 wt.%), Na_2O (1.8–4.7 wt.%), K_2O (3.7–6.5 wt.%), TiO_2 (0.4–1.2 wt.%), and P_2O_5 (0.02–0.5 wt.%); they have relatively high concentrations of Zr (700–1647 ppm) (Table 2). The mylonitic syenites are enriched in REE (750–1081 ppm) compared with the undeformed syenites (236–346 ppm; Table 2; Fig. 10A). However, the mylonitic syenites have trace element compositions that are quite different from those of the undeformed syenites. For example, the chondrite-normalized REE patterns of the mylonitic syenites are less fractionated (La_N/Yb_N = 10.2–17.0) than those of the

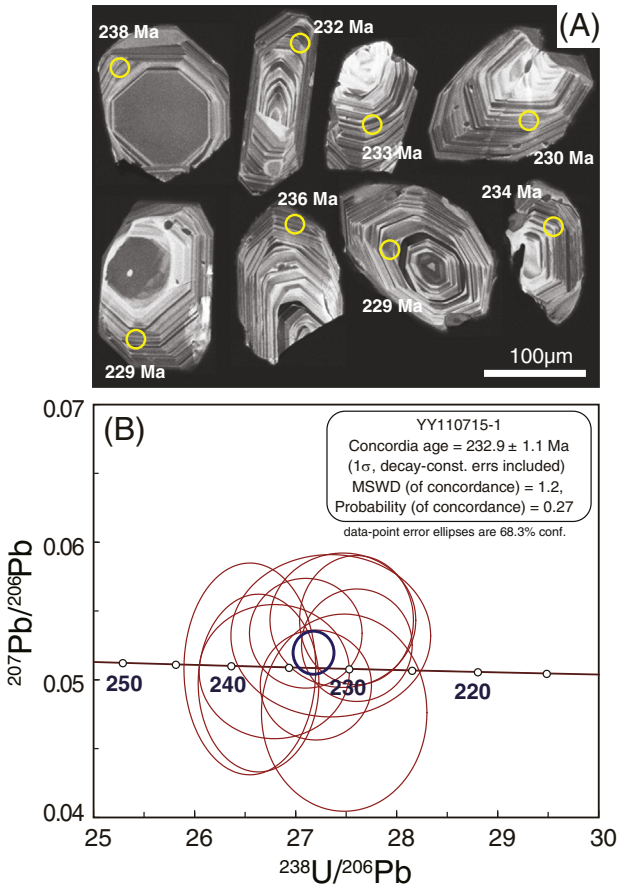

Fig. 9. Intrusion age of syenite. (A) Cathodoluminescence (CL) image of dated zircon grains from the Yangyang syenite. (B) ^{206}Pb–^{238}U ages, and U–Pb concordia diagram for the Yangyang syenite.

undeformed syenites (12–29), and exhibit pronounced negative Eu anomalies (Eu/Eu* = 0.3–0.8) (Fig. 10). Primitive-mantle-normalized multi-element plots of the mylonitic syenites exhibit distinctly negative Ba, Sr and P anomalies, and enrichments in Nb, Ta, Zr, and Hf relative to undeformed syenite (Fig. 10B).

Alteration products show a wide compositional range in SiO_2 (40.1–70.0 wt.%), Al_2O_3 (3.2–18.8 wt.%), $Fe_2O_3^{tot}$ (4.4–20.0 wt.%), CaO (1.9–19.6 wt.%), Na_2O (0.5–4.8 wt.%), K_2O (0.5–6.5 wt.%), TiO_2 (0.1–10.3 wt.%), P_2O_5 (0.01–2.8 wt.%), and Mg# (25.5–70.6) (Table 2).

Weak Ca (–Na) alteration occurred over a wide area of the cataclastic and mylonitic syenite. Samples from these alteration products display relative enrichment in HREE (La_N/Yb_N = 3.3) compared with the unaltered syenite and marked negative Eu anomalies (Eu/Eu* = 0.4; Fig. 10C). All Ca alteration products have greater HREE enrichments (La_N/Yb_N = 5.1–22.2) than the Ca (–Na) alteration products, and have slightly less negative Eu anomalies (Eu/Eu* = 0.4–0.7). Ca–K alteration products have La_N/Yb_N = 6.9–37.6 and variable Eu/Eu* (0.4–1.1; Table 2; Fig. 10E). The K alteration products yield La_N/Yb_N = 17.4–48.2 and Eu/Eu* = 1.1. Phyllic alteration products yield La_N/Yb_N = 10.6 and Eu/Eu* = 0.8 (Table 2; Fig. 10G). Total REE concentrations are relatively high in the products of Ca alteration (373–5143 ppm), Ca–K alteration (231–1118 ppm), and K alteration (281–631 ppm), compared with lower total REE concentrations in the products of Ca (–Na) alteration (300 ppm) and phyllic alteration (281 ppm) (Table 2). The high total REE concentrations in altered syenites are welled with the high REE in the sphenes and apatites (Table 2).

The compositional variations of the altered rocks reflect the effects of hydrothermal alteration after ductile and/or brittle deformation (Fig. 11). Sphene and apatite are abundant in the alteration zones and occur with amphibole and biotite; the sphene occurs mainly in Ca and Ca–K alteration products, while the apatites are more abundant in the Ca–K and K alteration products. The Ca and Ca–K alteration products have variable TiO_2 concentrations (0.1–10.3 wt.%) that are controlled by their sphene content. The high Ca concentrations in Ca–K alteration products are possibly controlled by a combination of amphibole and sphene (Fig. 11A), whereas their high P_2O_5 concentrations (0.02–2.74 wt.%) reflect abundant apatite (Fig. 11C). In particular, two sphene-rich samples (YY1003-16 and YY1003-18) with obvious Ca alteration have extremely high TiO_2 concentrations (5.7–10.3 wt.%; Fig. 4G) and relatively high Nb (528–909 ppm), Ta (44–221 ppm), and $\sum$REE (2862–5143 ppm) (Table 2; Fig. 10D). This geochemistry is a result of the high REE concentration in sphene.

Biotite grains in the syenite are dark brown, while biotites are green to pale yellow in the alteration zones and pale brown in the ores (Fig. 5E, F, G). Dark brown biotites in the Yangyang syenites have a Mg# of 0.47–0.53, FeO = 18.4–21.9 wt.%, TiO_2 = 1.6–1.9 wt.%, and Al_2O_3 = 15.5–16.1 wt.%. The green to pale yellow alteration-zone biotites have a higher Mg# of 0.6–0.8 and low FeO (10.6–17.3 wt.%), TiO_2 (0.4–1.3 wt.%), and Al_2O_3 (11.4–13.8 wt.%). The pale brown biotites in the ores are chemically similar to those in the alteration zone, with Mg# of 0.6–0.8, FeO = 10.4–18.5 wt.%, TiO_2 = 0.3–2.0 wt.%, and Al_2O_3 = 11.9–14.2 wt.%. Thus, a decrease in Ti, Fe, and Al concentrations corresponds to an increase in Mg and Si. This indicates that secondary sphene was generated by the dissolution of primary biotite during alteration of the syenite and gneiss.

5.2. LA-ICP-MS U–Pb geochronology and trace element chemistry of sphene

Sphene with various morphologies is a common accessory mineral within the syenites, their alteration products, and the ores in the Yangyang deposit. The sphene is mostly euhedral to subhedral in the syenite, whereas it occurs as aggregates or isolated rounded grains in the alteration products (Figs. 5D, 12A) and as irregular grains surrounding magnetite in the ores (Fig. 5G).

Sphene is most abundant in the Ca and Ca–K alteration products, where it occurs in association with amphibole, biotite, and apatite. These sphenes have enriched LREE patterns (La_N/Yb_N = 8.4–25.4) without distinct Eu anomalies (Eu/Eu* = 0.7–1.3; Table 5; Fig. 12B), although they have variable total REE concentrations. Sphenes from the alteration products, iron orebodies, and cataclastic syenite have dark and bright domains in the backscattered electron (BSE) images (Figs. 12A, 13A). The dark cores and bright rims of sphenes in the alteration products and iron orebodies reflect differences in REE enrichment (Fig. 12A); the bright domains are consistently enriched in LREE, V, Zr, Y, Th, and U compared with neighboring dark domains (Table 5). The LA-ICP-MS U–Pb age obtained from these sphenes records Fe mineralization at 215.7 ± 2.8 Ma (Table 7; Fig. 12C).

BSE images of euhedral to subhedral sphenes in the cataclastic syenites show bright cores and dark rims (Fig. 13A), which both display similar patterns of LREE depletion (especially La and Ce) and variably negative Eu anomalies (La_N/Yb_N = 1.0–18.4, Eu/Eu* = 0.5–1.0; Table 5; Fig. 13B). Sphenes in the cataclastic syenite yield a LA-ICP-MS U–Pb age of 207.6 ± 3.4 Ma (Table 8; Fig. 13C). We interpret this age as having been reset as a result of elemental redistribution during alteration by hydrothermal fluids, probably derived from younger Jurassic and Cretaceous intrusions.

Kim (2014) reported an LA-ICP-MS U–Pb age of 220 ± 5.2 Ma for euhedral sphene from the alteration zone, which is broadly consistent with our igneous SHRIMP U–Pb zircon age of 232.9 ± 1.1 Ma from the syenite. These older ages represent the timing of syenite emplacement, prior to multiple deformation and hydrothermal events.

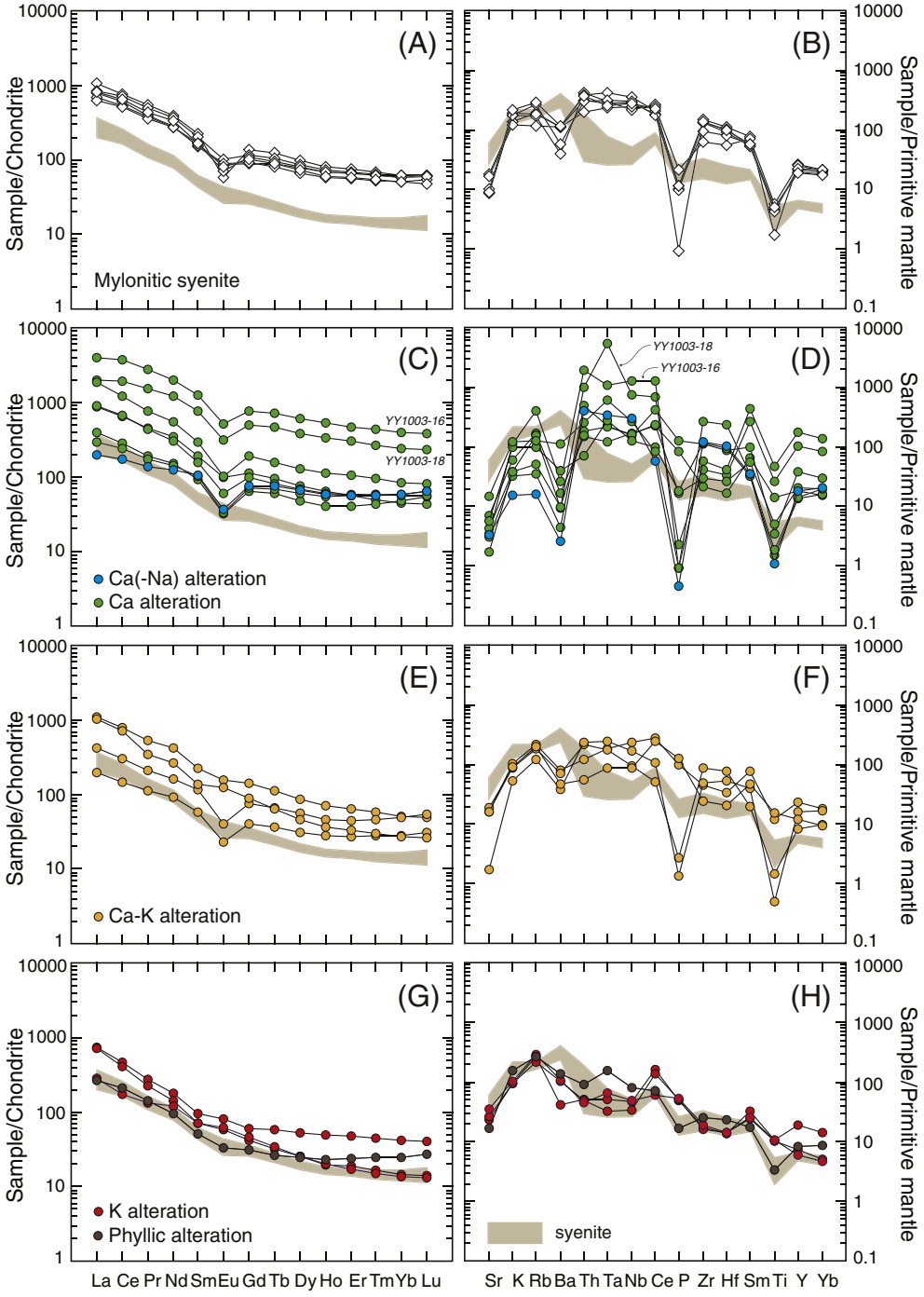

Fig. 10. Chondrite-normalized REE patterns and primitive-mantle-normalized trace element patterns of altered rocks. (A, B) mylonitic syenite. (C, D) Ca (–Na) and Ca alteration products. (E, F) Ca–K alteration products. Two Ca-altered samples (YY1003-16 and YY1003-18) have anomalously high concentrations of sphene (5–10 vol.%). (G, H) K and phyllic alteration products.

5.3. LA-ICP-MS U–Pb geochronology and trace element chemistry of apatite

Apatite is closely related to the iron mineralization and can be subdivided into two types based on its occurrence and chemical characteristics: Type-I apatites occur with magnetite ores or magnetite–pyrite ores (Figs. 6A, 12D), while Type-II apatites are rimmed by allanite and occur in the magnetite ores or alteration zone (Figs. 6B, 13D). The Type-I apatites can be further subdivided into Type-Ia and Type-Ib according to textural features such as grain shape and the presence or absence of inclusions. Type-Ia apatites are coarse grained (>1 mm) and contain abundant inclusions of Th-poor monazite, allanite, magnetite, actinolite, sulfides, and fluid. The rims of Type-Ia apatites are embayed and corroded (Fig. 6C, E). In comparison, Type-Ib apatites are fine grained (<500 μm) and rarely contain inclusions. Most Type-I apatite is fluorapatite with average and maximum F concentration of 3.7 and 6.5 wt.%, respectively. Both varieties of Type-I apatites have enriched LREE patterns and negative Eu anomalies (La_N/Yb_N = 29.6–110.7, Eu/Eu^* = 0.3–0.7; Table 6; Fig. 12E). Both Type-Ia and

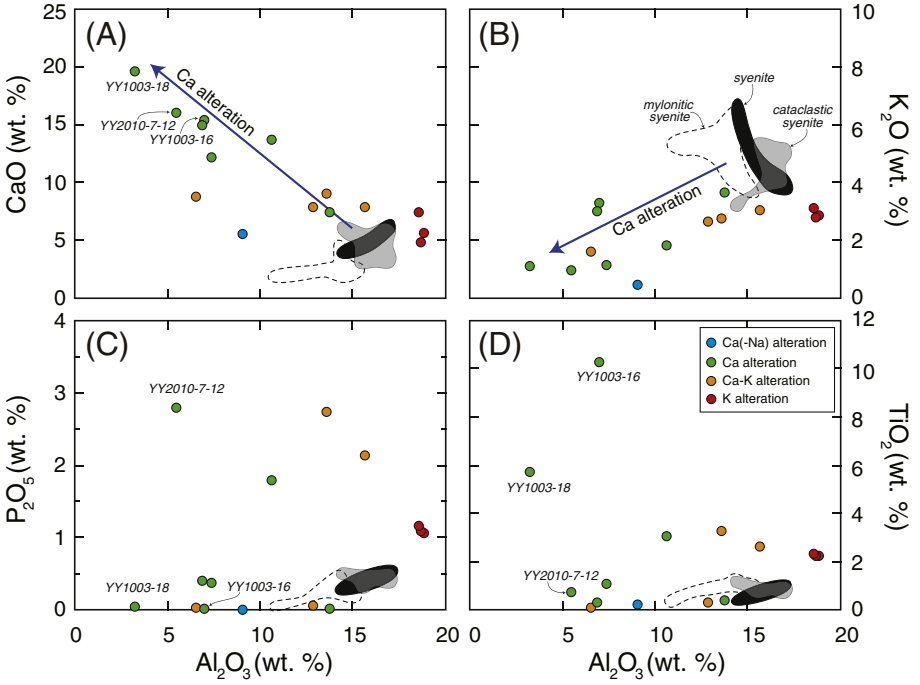

Fig. 11. Whole-rock major element geochemistry of altered rocks, compared with the fields for syenites. Concentrations are plotted with Al_2O_3 (wt.%). Fresh syenite (black field) and cataclastic syenite (gray field) have similar chemical compositions, while the field of mylonitic syenite (dashed line) is slightly offset from them. Sphene and apatite are abundant in the alteration zones and occur with amphibole and biotite. The high Ca and Ti concentrations (A, D) in Ca and Ca–K alteration products reflect the presence of sphene. Amphibole probably also contributes Ca to the Ca–K alteration products. The high Ca and P concentrations (A, C) in the Ca–K and K alteration products reflect the presence of abundant apatite. The high K concentrations (B) in Ca–K and K alteration products are probably controlled by biotite.

Type-Ib apatite exhibit dark and bright domains in BSE images (Figs. 6D, 12D). The dark domains are consistently depleted in REE, Si, Y, Th, and U compared with adjacent bright domains (Table 6). The LA-ICP-MS U–Pb age of Type-I apatites is 212 ± 13 Ma, which records the age of Fe mineralization (Table 9; Fig. 12F). The halite-bearing fluid inclusions within Type-Ia apatite provide evidence regarding the evolution of the hydrothermal system from saline fluids (Fig. 6E, F); however, the fluid inclusions are too small to allow measurements of the homogenization temperature and salinity.

Type-II apatites are mantled by allanite (Fig. 13D), which suggests that REEs within the apatite were remobilized into the allanite. The REE pattern of altered apatites is relatively low in LREE (La_N/Yb_N = 4.2–12.9) compare with the unaltered Type-I apatites, and displays negative Eu anomalies (Eu/Eu^* = 0.27–0.31; Table 6; Fig. 13E). It should be noted that depletion relative to Type-I apatites is greater for LREE than for HREE, which suggests an interaction between the apatites and hydrothermal fluids (Bonyadi et al., 2011; Harlov et al., 2002). These Type-II apatites yield a LA-ICP-MS U–Pb age of 151 ± 13 Ma (Table 10; Fig. 13F), which is younger than the age of the Type-I apatites and indicates resetting of the isotope system. This age, combined with the evidence for remobilization of hydrothermal fluids, suggests a second hydrothermal episode during the intrusion of Jurassic and Cretaceous plutonic rocks. Similar events have been described elsewhere. For example, the mineral chemistry is recorded in apatites by remobilized hydrothermal fluids in the Kiruna area of Sweden and in the Bafq district of Iran (Harlov et al., 2002; Torab and Lehmann, 2007).

5.4. Geochemistry of ores and LA-ICP-MS trace element chemistry of magnetite

The magnetites in these rocks are commonly recrystallized, have triple-junction grain boundaries, and are locally partly martitized. The Yangyang ores can be subdivided into two major groups based on mineralogy and geochemistry: 1) magnetite-type ore and 2) magnetite–pyrite-type ore. Most ore samples have variable P_2O_5 and $Fe_2O_3^{tot}$ concentrations (0.01–7.4 wt.% and ~20–90 wt.%, respectively). The whole-rock Ti concentration of the magnetite-type ore ranges from 3437 to 20605 ppm, and V concentrations range from 130 to 404 ppm, while the whole-rock Ti concentration of the magnetite–pyrite-type ore ranges from 138 to 521 ppm and V concentrations range from 89 to 211 ppm (Fig. 14A).

Magnetite grains in the magnetite-type ore and in the magnetite–pyrite-type ore generally contain much lower Ti (249–2409 ppm, 428–760 ppm) and V concentrations (367–1011 ppm, 208–252 ppm), respectively (Table 11; Fig. 14B).

Generally, magnetite displays different trace element concentrations depending on the environment in which it forms (Fig. 14). Therefore, we compare the whole-rock (ore) geochemistry and ore mineral (magnetite) chemistry based on Ti and V contents (Fig. 14A, B; Loberg and Horndahl, 1983). The whole-rock geochemistry of the magnetite-type ores that lack sphene and the magnetite–pyrite-type ores plot in the apatite–magnetite ores field on the compositional diagram; however, sphene-bearing magnetite-type ores plot in the titaniferous iron-oxide ore field (nelsonites) because of their abundance of sphene (Fig. 14A). In keeping with this whole-rock geochemistry, all of the magnetite minerals from magnetite-type ore fall within the apatite–magnetite ore field (Fig. 14B).

6. Discussion

6.1. Age of iron mineralization and alteration, and relation to the Yangyang deposit

The LREE-rich sphenes and apatites in the Yangyang orebodies and alteration products yield mineralization ages of 212–215 Ma. The

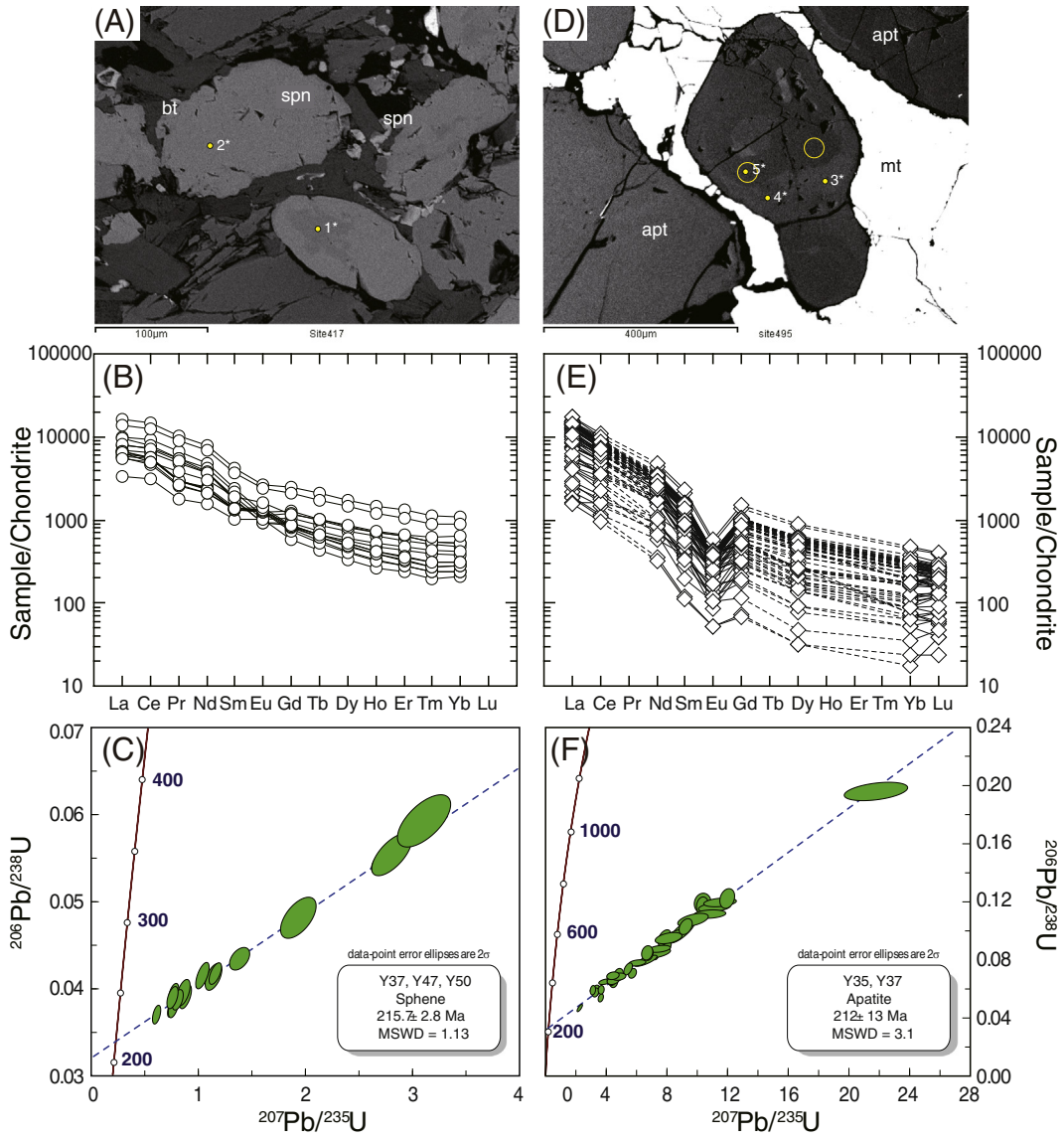

Fig. 12. Iron mineralization ages within the Ca–K alteration zone. (A) BSE image of analyzed sphene. 1* and 2* refer to individual analyses of bright and dark domains of sample Y47, respectively, reported in Table 4. (B) Chondrite-normalized REE pattern of sphenes within the Ca–K alteration zones and magnetite ores. (C) U–Pb concordia diagram for Ca–K alteration sphenes. (D) BSE image of analyzed apatites within the magnetite ores. 3*–5* refer to individual analyses of bright and dark domains of sample Y35, respectively, as reported in Table 7. (E) Chondrite-normalized REE pattern of apatites within the magnetite and magnetite–pyrite ores. (F) U–Pb concordia diagram for apatites.

LREE-depleted dark-rimmed sphene and alanite-rimmed apatite have younger ages (207.6 ± 5.2 Ma and 151 ± 13 Ma), indicating remobilization of their elements during secondary hydrothermal overprinting. This is consistent with previous observations in other IOA deposits including the Kiruna area of Sweden and the Bafq district of Iran (Harlov et al., 2002; Torab and Lehmann, 2007). The younger ages of 207 and 151 Ma suggest that multiple resetting events occurred as a result of hydrothermal alteration during the intrusion of the Jurassic Osaek granite (189–199 Ma) and the Cretaceous Sokcho-Seolak granite (84–90 Ma) in the Yangyang region (Song et al., 2011). These post-mineralization igneous activities may have reset the U–Pb isotope system of sphene and apatite to younger ages. The constraints on the ages of these events are shown in Fig. 15.

Integration of the mineralogy, geochemistry, and fluid inclusion data with the geochronological data suggests that the Yangyang magnetite–apatite ores formed by magmatic hydrothermal alteration in a Triassic post-collisional tectonic setting. This interpretation is inconsistent with previous studies (James et al., 2005; Kim, 1977; Lee, 1968; Lee and Kim, 1968; Lee and Stout, 1989; So, 1978). The paragenetic sequence of the Yangyang deposit can be interpreted in terms of the following alteration sequence: an early sodic alteration (albite) → calcic alteration (amphibole) → potassic alteration (biotite) → phyllic alteration (sericite). The iron-oxide mineralization mainly accompanied the Ca and K alterations. These poly-alteration patterns are equivalent to those of the Kiruna-IOA deposits in Sweden (Romer, 1994) and the mineral assemblages are similar to those of IOCG-type deposits in Chile (Edfelt et al., 2005; Williams et al., 2005). Generally, IOCG (IOA)-type deposits record sodic alteration; however, the Yangyang deposit experienced only weak sodic alteration and strong calcic and potassic alterations. This suggests that there was no source for Na, such as evaporites, whereas the Ca and K components were supplied from syenites and hydrothermal fluids derived from deeply hidden magmatic sources. The abundant sphene is also consistent with a Ca-rich hydrothermal fluid, which was enriched with Ti

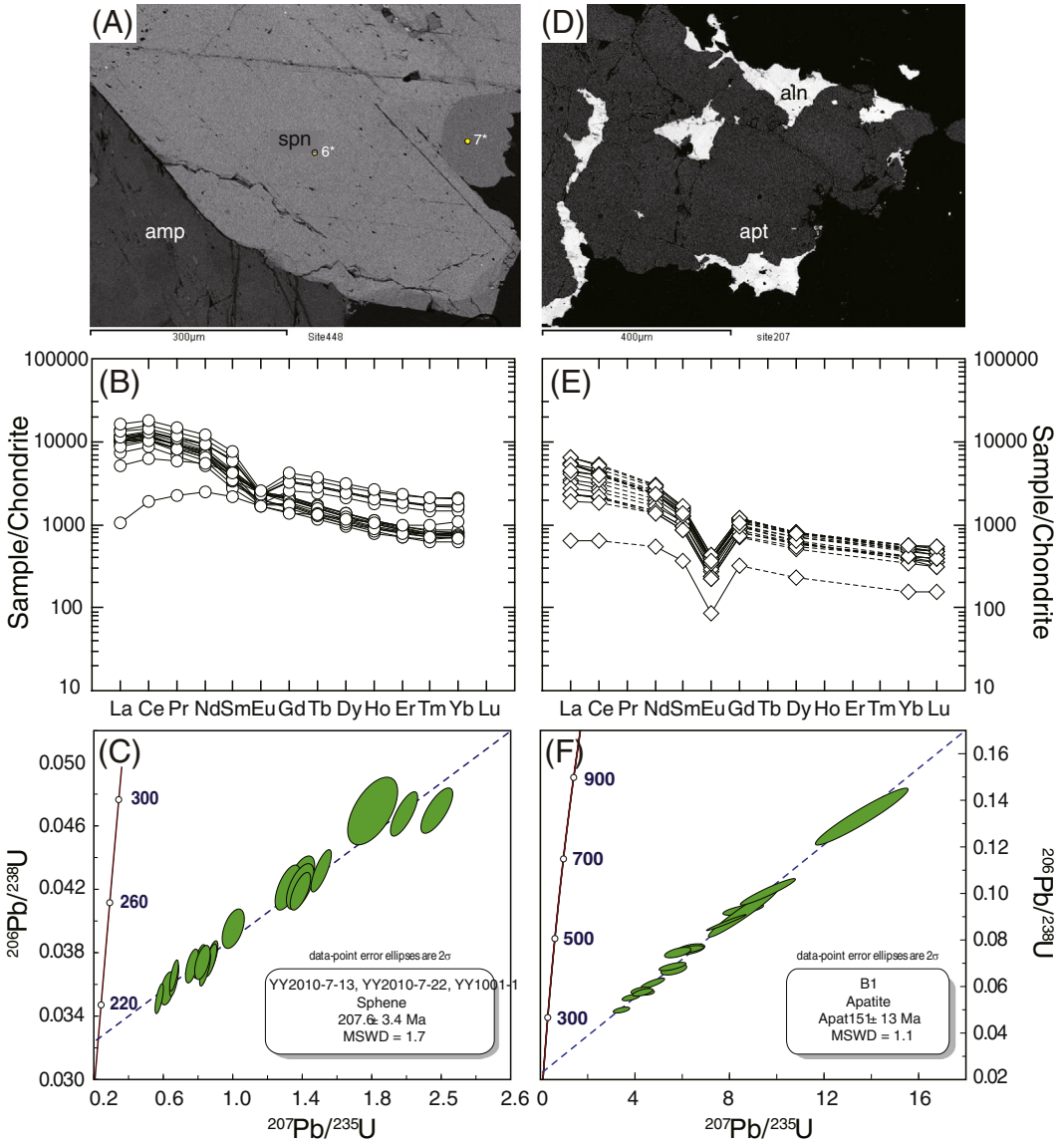

Fig. 13. Age of post-igneous alteration of cataclastic syenite. (A) BSE image of analyzed sphene. 6* and 7* refer to individual analyses of bright and dark domains of sample YY2010-7-13, respectively, as listed in Table 4. (B) Chondrite-normalized REE patterns of sphenes from cataclastic syenite. (C) U–Pb concordia diagram for sphenes from cataclastic syenite. (D) BSE image of analyzed apatite within the magnetite ores. (E) Chondrite-normalized REE patterns of apatites. (F) U–Pb concordia diagram for apatites.

that leached out from biotite-bearing country rocks such as syenite and/or gneiss.

The apatite grains commonly contain inclusions of Th-poor monazite, magnetite, and sulfides. They also exhibit patchy zoning that formed by interaction between apatite and hydrothermal fluid, resulting in lighter domains with high concentrations of REE and some trace elements such as Si, S, Y, Pb, Th, and U. Furthermore, the halite-bearing fluid inclusions in the apatite indicate that the hydrothermal system evolved from saline fluids. The Yangyang magnetite–apatite ores probably precipitated from saline magmatic-hydrothermal fluids. This hydrothermal overprint on apatite has been observed in other IOA deposits, such as the Kiruna deposit in Sweden and the Bafq deposit in Iran (Harlov et al., 2002; Torab and Lehmann, 2007).

6.2. Origin of the Yangyang iron-oxide–apatite (IOA) deposit

Studies over the past 50 years have suggested that the Yangyang deposit formed by contact metasomatism (skarnification; James et al., 2005), orthomagmatism (Lee, 1968), metamorphism of iron-rich sediment (So, 1978), or alkali metasomatism (Kim, 1977; Lee and Kim, 1968; Lee and Stout, 1989). However, previous studies ignored the influence of structure and lithology on the location of iron orebodies. An important point that has previously been overlooked is that the 'metasedimentary' rocks or amphibolites reported in previous studies are not the products of regional metamorphism. Instead, they are syenites that have been deformed and altered by ductile and brittle deformation, and subsequently hydrothermally altered within the shear zone. The Yangyang iron orebodies occur within a mylonitic shear zone in the syenite that has been overprinted by cataclastic deformation. The orebodies resulted from a series of alterations caused by the injection of hydrothermal fluid along the shear zone. In many cases, the iron orebodies occur as structurally controlled lenses along the shear zone. We therefore propose the following model to explain the formation of the Yangyang IOA deposit in association with multiple alteration episodes (Fig. 16): (1) Triassic post-collisional intrusion of the syenite; (2) ductile

Table 7
LA-ICP-MS U–Pb age data for sphene from syenite and alteration products in the Yangyang area, South Korea.

Spot	$^{206}Pb/^{238}U$	±1σ	$^{207}Pb/^{235}U$	±1σ	$^{207}Pb/^{206}Pb$	±1σ	$^{208}Pb/^{232}Th$	±1σ	Age (Ma)
Sample: Y37									215.7 ± 2.8
1	0.04813	0.00097	1.9400	0.0679	0.2923	0.0084	0.01798	0.00035	
2	0.03794	0.00052	0.7728	0.0203	0.1478	0.0033	0.01371	0.00013	
3	0.04135	0.00062	1.1468	0.0319	0.2012	0.0047	0.01582	0.00023	
4	0.05541	0.00099	2.8141	0.0757	0.3684	0.0074	0.03600	0.00074	
5	0.03953	0.00062	0.8664	0.0258	0.1590	0.0040	0.01340	0.00013	
6	0.05926	0.00123	3.1162	0.1020	0.3814	0.0097	0.02841	0.00073	
Sample: Y47									
1	0.03947	0.00046	0.7758	0.0186	0.1426	0.0030	0.02805	0.00057	
2	0.04148	0.00062	1.0437	0.0248	0.1825	0.0034	0.02486	0.00035	
3	0.03871	0.00048	0.8138	0.0215	0.1525	0.0035	0.02134	0.00026	
4	0.03700	0.00044	0.6151	0.0151	0.1206	0.0026	0.01784	0.00021	
5	0.03897	0.00052	0.7651	0.0202	0.1424	0.0032	0.02214	0.00034	
6	0.04172	0.00050	1.1645	0.0232	0.2024	0.0032	0.02749	0.00041	
7	0.04344	0.00053	1.3935	0.0386	0.2327	0.0058	0.03690	0.00066	
Sample: Y50									
1	0.05481	0.00068	2.7717	0.0589	0.3668	0.0063	0.02763	0.00034	
2	0.03781	0.00045	0.7566	0.0154	0.1451	0.0024	0.01377	0.00011	
3	0.03907	0.00057	0.8838	0.0229	0.1641	0.0035	0.01482	0.00018	

Table 8
LA-ICP-MS U–Pb age data for sphene from syenite in the Yangyang area, South Korea.

Spot	$^{206}Pb/^{238}U$	±1σ	$^{207}Pb/^{235}U$	±1σ	$^{207}Pb/^{206}Pb$	±1σ	$^{208}Pb/^{232}Th$	±1σ	Age (Ma)
Sample: YY20107-13									207.6 ± 3.4
1	0.04693	0.00087	1.8099	0.0591	0.2797	0.0075	0.02183	0.00037	
2	0.04266	0.00058	1.3946	0.0325	0.2371	0.0045	0.02004	0.00017	
3	0.03574	0.00043	0.6263	0.0166	0.1271	0.0030	0.03251	0.00077	
4	0.03951	0.00051	1.0045	0.0260	0.1844	0.0042	0.02090	0.00036	
5	0.04210	0.00058	1.3189	0.0295	0.2272	0.0040	0.01469	0.00014	
6	0.04216	0.00059	1.3917	0.0325	0.2394	0.0045	0.01479	0.00015	
7	0.03744	0.00043	0.8125	0.0147	0.1574	0.0022	0.01282	0.00008	
Sample: YY20107-22									
1	0.04674	0.00057	1.9907	0.0321	0.3089	0.0032	0.01790	0.00025	
2	0.04315	0.00054	1.5116	0.0243	0.2541	0.0026	0.01479	0.00012	
3	0.03772	0.00042	0.8814	0.0143	0.1695	0.0020	0.01428	0.00010	
4	0.03750	0.00042	0.8751	0.0141	0.1692	0.0020	0.01427	0.00010	
5	0.04695	0.00058	2.1796	0.0369	0.3367	0.0039	0.01582	0.00017	
6	0.04188	0.00049	1.3923	0.0239	0.2411	0.0031	0.01443	0.00011	
Sample: YY1001-1									
1	0.03626	0.00042	0.6649	0.0110	0.1330	0.0016	0.01328	0.00011	
2	0.03695	0.00043	0.8426	0.0131	0.1654	0.0017	0.01357	0.00011	
3	0.03714	0.00044	0.7676	0.0155	0.1499	0.0025	0.01260	0.00007	
4	0.03655	0.00040	0.6650	0.0105	0.1320	0.0015	0.01285	0.00008	
5	0.03509	0.00039	0.5787	0.0093	0.1196	0.0014	0.01245	0.00007	
6	0.03738	0.00044	0.8273	0.0186	0.1605	0.0031	0.01304	0.00010	

Table 9
LA-ICP-MS U–Pb age data for apatites from ore and alteration products in the Yangyang area, South Korea.

Spot	$^{206}Pb/^{238}U$	±1σ	$^{207}Pb/^{235}U$	±1σ	$^{207}Pb/^{206}Pb$	±1σ	$^{208}Pb/^{232}Th$	±1σ	Age (Ma)
Sample: Y35									212 ± 13
1	0.0590	0.0015	3.30	0.27	0.4080	0.0360	0.01430	0.00150	
2	0.0967	0.0036	8.42	0.70	0.6410	0.0540	0.01670	0.00180	
3	0.0649	0.0015	3.96	0.34	0.4410	0.0390	0.01420	0.00150	
4	0.1195	0.0024	11.52	0.89	0.6910	0.0580	0.02370	0.00250	
5	0.0689	0.0019	4.63	0.38	0.4870	0.0430	0.01560	0.00160	
6	0.0948	0.0032	8.13	0.71	0.6230	0.0560	0.02150	0.00240	
7	0.1074	0.0038	9.74	0.82	0.6600	0.0560	0.02000	0.00200	
8	0.0874	0.0019	7.53	0.59	0.6240	0.0520	0.01720	0.00180	
9	0.1221	0.0055	12.00	0.40	0.7050	0.0290	0.01828	0.00046	
10	0.0589	0.0030	3.37	0.20	0.4080	0.0260	0.01431	0.00036	
11	0.0574	0.0026	3.32	0.18	0.4230	0.0220	0.01414	0.00033	
12	0.0467	0.0021	2.29	0.14	0.3630	0.0210	0.01148	0.00035	
13	0.0593	0.0025	3.69	0.16	0.4520	0.0210	0.01387	0.00038	
14	0.0590	0.0027	3.15	0.16	0.3900	0.0220	0.01324	0.00028	
15	0.0837	0.0035	6.82	0.23	0.5820	0.0210	0.01617	0.00040	
16	0.0654	0.0037	4.52	0.23	0.4920	0.0360	0.01546	0.00038	
17	0.0697	0.0035	4.84	0.25	0.5040	0.0290	0.01454	0.00033	
18	0.0736	0.0034	5.46	0.23	0.5410	0.0230	0.01540	0.00037	
19	0.0666	0.0035	4.36	0.23	0.4760	0.0290	0.01420	0.00034	
20	0.0658	0.0024	4.49	0.33	0.5030	0.0330	0.01420	0.00120	
21	0.0683	0.0021	4.87	0.38	0.5370	0.0360	0.01460	0.00120	
22	0.0689	0.0021	4.47	0.33	0.4740	0.0320	0.01520	0.00120	
23	0.1027	0.0045	9.24	0.35	0.6440	0.0250	0.01692	0.00038	
24	0.0847	0.0040	6.72	0.30	0.5690	0.0260	0.01581	0.00036	
Sample: Y37									
1	0.1190	0.0055	10.36	0.44	0.6240	0.0350	0.02514	0.00070	
2	0.1169	0.0051	10.38	0.33	0.6420	0.0290	0.02362	0.00054	
3	0.0897	0.0036	8.00	0.25	0.6440	0.0210	0.02153	0.00047	
4	0.0844	0.0036	7.25	0.22	0.6210	0.0230	0.02059	0.00046	
5	0.0706	0.0028	5.76	0.22	0.5880	0.0220	0.01907	0.00040	
6	0.0997	0.0067	9.01	0.71	0.6470	0.0300	0.02370	0.00110	
7	0.0951	0.0045	7.85	0.34	0.5990	0.0240	0.01822	0.00057	
8	0.0537	0.0022	3.67	0.14	0.4880	0.0170	0.01648	0.00038	
9	0.1958	0.0052	21.80	1.70	0.8070	0.0690	0.04480	0.00460	
10	0.0843	0.0025	7.50	0.62	0.6540	0.0560	0.01640	0.00170	
11	0.0793	0.0031	6.62	0.60	0.6020	0.0520	0.01480	0.00150	
12	0.0778	0.0018	6.08	0.47	0.5660	0.0480	0.02010	0.00210	
13	0.1162	0.0026	11.17	0.87	0.7160	0.0600	0.02510	0.00260	
14	0.1115	0.0024	10.85	0.85	0.7130	0.0610	0.02330	0.00240	

deformation and mylonitization of the syenite in a deep-crustal shear zone; (3) brittle deformation during exhumation, resulting in cataclastic overprinting of ductilely deformed syenite; and (4) repeated infiltration of hydrothermal fluid along the brittle–ductile shear zone, resulting in several stages of alteration. The injection of the ore-forming fluids along a structurally weak zone with crushed particles enhanced the fluid–rock interactions.

This first discovery of IOA-type mineralization on the Korean Peninsula is genetically related to Triassic post-collisional magmatism within the Gyeonggi Massif, South Korea.

Table 10
LA-ICP-MS U–Pb age data for allanite-rimmed apatite from magnetite ore in the Yangyang area, South Korea.

Spot	$^{206}Pb/^{238}U$	±1σ	$^{207}Pb/^{235}U$	±1σ	$^{207}Pb/^{206}Pb$	±1σ	$^{208}Pb/^{232}Th$	±1σ	Age (Ma)
Sample: B1									151 ± 13
1	0.05750	0.00110	4.43	0.34	0.5680	0.0480	0.03760	0.00410	
2	0.06130	0.00180	4.77	0.41	0.5630	0.0480	0.03950	0.00440	
3	0.05800	0.00130	4.26	0.33	0.5320	0.0440	0.03480	0.00360	
4	0.04980	0.00100	3.45	0.29	0.5100	0.0440	0.03210	0.00360	
5	0.07590	0.00190	6.36	0.50	0.6180	0.0520	0.04440	0.00480	
6	0.09300	0.00200	8.60	0.70	0.6810	0.0570	0.06500	0.00720	
7	0.09160	0.00860	8.60	1.20	0.6710	0.0620	0.06280	0.00890	
8	0.06720	0.00190	5.66	0.45	0.5950	0.0510	0.04790	0.00520	
9	0.13300	0.01000	13.60	1.60	0.7490	0.0630	0.10600	0.01600	
10	0.06850	0.00150	5.61	0.46	0.6010	0.0500	0.04800	0.00530	
11	0.10060	0.00470	9.63	0.95	0.6830	0.0580	0.08900	0.01100	
12	0.05520	0.00120	3.85	0.31	0.5080	0.0430	0.02510	0.00270	
13	0.08740	0.00280	7.87	0.68	0.6500	0.0540	0.04750	0.00560	
14	0.07590	0.00130	6.33	0.49	0.6030	0.0500	0.05320	0.00560	
15	0.07450	0.00180	5.83	0.46	0.5770	0.0490	0.04340	0.00440	
16	0.05740	0.00140	4.35	0.35	0.5510	0.0470	0.02950	0.00320	

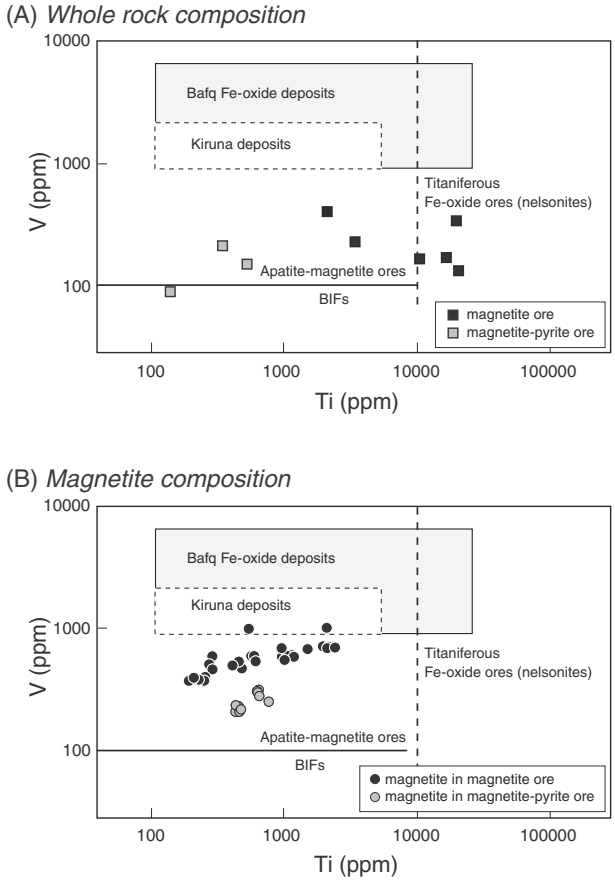

Fig. 14. Major and trace element discrimination diagrams for ore rocks and minerals (reference fields are after Loberg and Horndahl, 1983), compared with fields for the Kiruna deposit in Sweden (Nystrom and Henriquez, 1994) and Fe-oxide deposits in the Bafq district, Iran (Daliran, 1990; Mosavi, 1994). (A) Whole-rock concentrations of titanium and vanadium for the Yangyang ores. (B) Titanium and vanadium concentrations of magnetite minerals from Yangyang deposit ore rocks. BIFs—banded iron formation.

7. Conclusions

Regional Fe–P mineralization in the Yangyang deposit resulted from the injection of magmatic, saline hydrothermal fluids through a shear zone within the host Triassic syenite. Multiple alteration episodes clearly overprint the ductile and/or brittle structural features. The alteration patterns show an evolutionary trend of overprinting by Ca (–Na), Ca, Ca–K, K, and phyllic alteration events. Sphene occurs mainly within the Ca and Ca–K alteration products, whereas apatite occurs mainly within Ca–K and K alteration products, and is accompanied by iron mineralization. The SHRIMP U–Pb zircon age and whole-rock chemistry of the Yangyang syenite indicates that it was intruded at 233 Ma in a post-collisional tectonic setting. After intrusion, the syenite body was ductilely deformed, followed by exhumation and brittle deformation. Fe–P mineralization developed along a weak shear zone during multiple successive alterations. The LA-ICP-MS U–Pb ages of sphene and apatite reveal that the Fe–P mineralization occurred at 220–210 Ma. Subsequent resetting occurred at 208–151 Ma when the U–Pb system was disturbed by Jurassic and Cretaceous magmatism.

Acknowledgments

This research was supported by a grant from the Korea Institute of Energy Technology Evaluation and Planning (KETEP; 2012T100201564). And this research was supported by Basic Science Research Program

Table 11
Representative results of LA-ICP-MS analyses of trace elements within magnetite in the Yangyang area, South Korea.

Rock type	Magnetite ore										Magnetite–pyrite ore			
Sample	YY201206-1-1		Y30		Y54		31	20	Y47[a]		YY22		YY2010A	98
Trace and rare earth elements (ppm)														
Ti	287.2	248.5	564.2	1180.8	952.9	2409.4	227.0	191.2	608.0	479.0	2084.0	540.0	624.0	648.0	427.8	470.8	760.0
V	591.9	366.9	594.2	585.3	691.1	698.6	381.2	372.9	537.7	470.1	1011.0	994.0	307.0	280.0	208.6	218.3	252.0
Si	1692.9	1734.4	1689.7	1782.3	2358.3	2768.2	1948.6	2050.4	1778.9	1714.8	b.d.	b.d.	2439.0	2166.0	1594.9	1616.2	1169.0
Al	991.7	1135.0	733.8	1080.7	1836.6	1605.6	1581.9	1142.1	959.5	539.4	3017.0	2435.0	232.0	220.0	141.2	135.4	582.0
Mg	115.8	189.8	45.4	233.4	658.0	335.4	196.0	152.6	145.7	39.4	222.0	194.0	795.0	702.0	730.4	789.5	217.0
Mn	1418.2	1229.7	1566.2	2119.8	1537.4	2192.2	1449.1	1236.7	1582.5	1354.5	1275.0	1374.0	1513.0	1631.0	1811.1	1517.2	1337.0
Zn	294.0	216.5	149.2	318.0	546.2	708.0	554.3	777.0	328.7	306.9	376.0	100.1	136.0	209.0	126.7	103.9	84.0
Ca	b.d.	27.7	b.d.	b.d.	27.7	862.4	b.d.	b.d.	b.d.	b.d.	b.d.	b.d.	b.d.	b.d.	b.d.	b.d.	b.d.
Ni	33.0	28.4	23.0	20.3	24.1	22.7	34.5	24.7	25.7	23.6	12.5	12.4	4.0	7.0	21.6	22.8	9.0
Cr	4.2	b.d.	1.4	1.1	7.4	8.6	0.7	0.7	1.6	2.3	6.0	4.0	8.0	6.0	8.6	3.7	1.0

Note: b.d. = below detection limits.
[a] Disseminated magnetite.

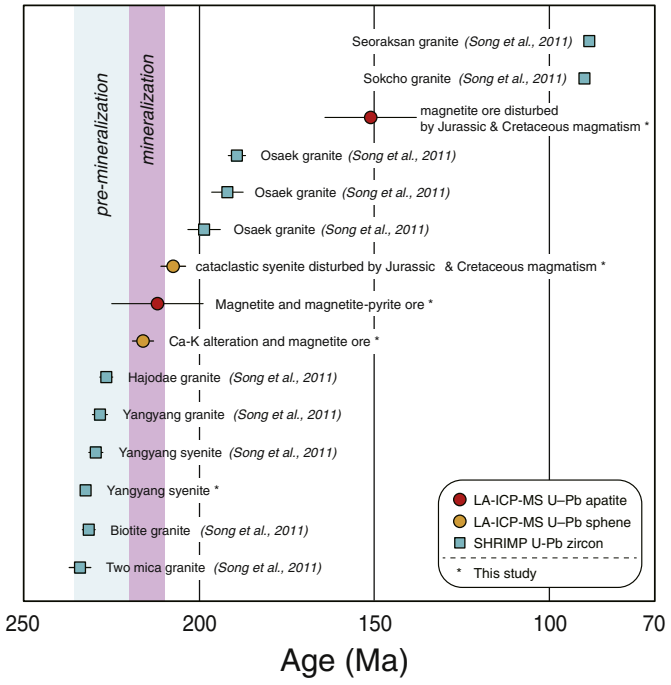

Fig. 15. Summary of geochronological data, showing the timing of intrusive, hydrothermal, and mineralization events in the Yangyang area.

through the National Research Foundation of Korea (NRF) funded by the Ministry of Science, ICT and Future Planning (2012R1A1A2005723, 20100027347). We thank Prof. Whattam for comments on the manuscript and the Korea Basic Science Institute for performing the SHRIMP analyses.

References

Allen, C.M., Campbell, I.H., 2012. Identification and elimination of a matrix-induced systematic error in LA-ICP-MS $^{206}Pb/^{238}U$ dating of zircon. Chem. Geol. 232, 157–165.
Black, L.P., Gulson, B.L., 1987. The age of the Mud Tank Carbonatite, Strangways Range, Northern Territory. BMR J. Aust. Geol. Geophys. 3, 227–232.
Bonyadi, Z., Davidson, G.J., Mehrabi, B., Meffre, S., Ghazban, F., 2011. Significance of apatite REE depletion and monazite inclusions in the brecciated Se-Chahun iron oxide–apatite deposit, Bafq district, Iran: insights from paragenesis and geochemistry. Chem. Geol. 281, 253–269.
Choi, S.G., Pak, S.J., Lee, P.K., Kim, C.S., 2004. An overview of geoenvironmental implications of mineral deposits in Korea. Econ. Environ. Geol. 37, 1–19.
Choi, S.G., Seo, J., Park, J.W., Kim, D.W., 2011. Mineralogy and Geochemistry of the Yangyang IOA Deposit, South Korea. Goldschmidt, Prague, Czech Republic (CD of abstracts).
Cox, K.G., Bell, J.D., Pankhurst, R.J., 1979. The Interpretation of Igneous Rocks. George Allen and Unwin, London (464 pp.).
Daliran, F., 1990. The Magnetite–Apatite Deposit of Mishdovan, East Central Iran. (Unpublished Ph.D. thesis), Ruprecht-Karls-Universitat, Heidelberg (248 pp.).
Duncan, R.J., Hitzman, M.W., Nelson, E.P., Togtokhbayar, O., 2014. Structural and lithological contrils on iron oxide copper–gold deposits of the southern Selwyn-Mount Dore corridor, Eastern Fold Belt, Queensland, Australia. Econ. Geol. 109, 419–456.
Edfelt, A., Armstrong, R.N., Smith, M., Martinsson, O., 2005. Alteration paragenesis and mineral chemistry of Tjarrojakka apatite–iron and Cu (–Au) occurrences, Kiruna area, northern Sweden. Mineral. Deposita 40, 409–434.
Harlov, D.E., Andersson, U.B., Foerster, H.J., Nystrom, J.O., Dulski, P., Broman, C., 2002. Apatite–monazite relations in the Kiirunavaara magnetite–apatite ore, northern Sweden. Chem. Geol. 191, 47–72.
Harris, N.B.W., Pearce, J.A., Tindle, A.G., 1986. Geochemical characteristics of collision zone magmatism. In: Coward, M.P., Reis, A.S. (Eds.), Collision Tectonics: Geological Society of London, Special Publication vol. 19, pp. 67–81.
James, L.P., Park, M.E., Burt, D.M., 2005. World skarn deposits: skarns of Asia outside of China and Japan. Economic Geology 100 Anniversary Volume. Society of Economic Geologist, Litteton, pp. 1–6 (Appendix 74).
Kim, H.S., 1977. Mineralogy and petrology of the Precambrian iron deposits, Korea. J. Geol. Soc. Korea 13, 191–211.
Kim, D.W., 2014. Mineralogical and Geochemical Characteristics of Hydrothermal Alteration in the Yangyang Iron Deposit. (Master Thesis), Korea Univ., Seoul, Korea (116 pp.).
Kim, O.J., Yun, H.I., Park, N.Y., 1958. Report of geological survey of Yangyang Mining District. Natl. Inst. Geol. Miner. 2, 47–74.
KORES, 2010. Detailed Geological Survey Report (Fe: Yangyang Area). Korea Resource Corporation (117 pp.).
Lee, E.D., 1968. Geology and exploration of mineral deposits in Yangyang mine. Min. Geol. 5, 45–54.

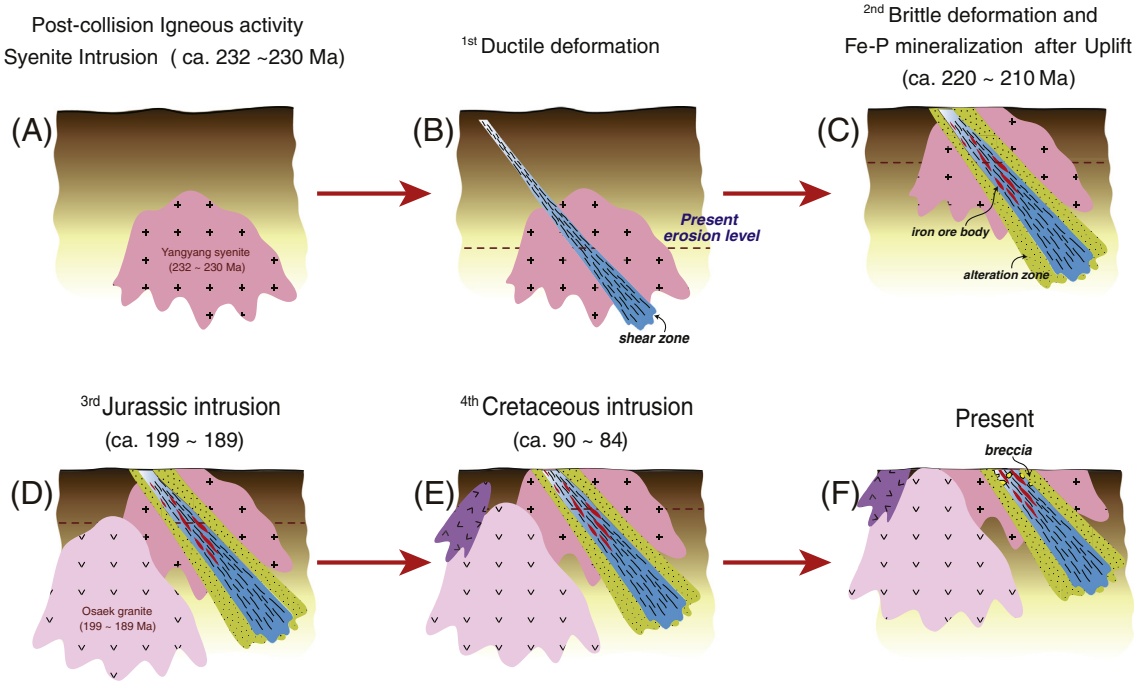

Fig. 16. Genetic model of the Yangyang IOA deposit. (A) Post-collisional Triassic magmatism. (B) Ductile deformation at depth, resulting in a foliation within the Yangyang syenite. (C) Cataclasis of the syenite during exhumation through the brittle crust was accompanied by Fe–P mineralization at ca. 220–210 Ma. (D) Overprint by Jurassic magmatism, such as intrusion of the Osaek granite at ca. 199–189 Ma. (E) Renewed magmatism in the Yangyang area during Cretaceous intrusion at ca. 90–84 Ma. (F) Erosion and exhumation to present levels.

Lee, S.H., 1987. Comparison of phase relationships of the host rocks and magnetite ore deposits in the Yangyang iron deposits, Korea. J. Geol. Soc. Korea 23, 242–256.
Lee, S.M., Kim, H.S., 1968. Petrogenesis and the syenite in the Yangyang mine district, Kangwon Province, Korea. J. Geol. Soc. Korea 4, 199–214.
Lee, S.H., Stout, J.H., 1989. Phase equilibria of coexisting minerals from amphibolites and syenitic rocks in the Yangyang magnetite deposit, Korea. J. Geol. Soc. Korea 25, 365–380.
Loberg, B.E., Horndahl, A.K., 1983. Ferried geochemistry of Swedish Precambrian iron ores. Mineral. Deposita 18, 487–504.
Longerich, H., Jackson, S.E., Gunther, D., 1996. Laser ablation inductively coupled plasma mass spectrometric transient signal data acquisition and analyte concentration calculation. J. Anal. At. Spectrom. 11, 899–904.
Ludwig, K.R., 2000. Isoplot/Ex version 2.4. A geochronological toolkit for Microsoft Excel. Berkeley Geochronological Centre Special Publication 1a. Berkeley Geochronological Centre, Berkeley, CA.
Miao, L.C., Qiu, Y., Mcnaughton, N., Luo, Z., Groves, D., Zhai, Y., Fan, W., Zhai, M., Guan, K., 2002. SHRIMP U–Pb zircon geochronology of granitoids from Dongping area, Hebei Province, China: constraints on tectonic evolution and geodynamic setting for gold metallogeny. Ore Geol. Rev. 19, 187–204.
Mosavi, N.Z., 1994. Geology and Genesis of Choghart Deposit, Bafq Area, Central Iran. (Unpublished M.Sc. Thesis), Shiraz University, Iran (192 pp., in Farsi).
Nystrom, J.O., Henriquez, F., 1994. Magmatic features of iron ores of the Kiruna-type in Chile and Sweden: ore textures and magnetite geochemistry. Econ. Geol. 89, 820–839.
Oh, C.W., Krishnan, S., Kim, S.W., Kwon, Y.W., 2006. Mangerite magmatism associated with a probable Late-Permian to Triassic Hongseong–Odaesan collision belt in South Korea. Gondwana Res. 9, 95–105.
Pearce, J.A., 1996. Source and setting of granitic rocks. Episodes 19, 120–125.
Pearce, J.A., Harris, N.B., Tindle, A.G., 1984. Trace element discrimination diagrams for the interpretation of granitic rocks. J. Petrol. 25, 957–983.
Peccerillo, A., Taylor, S.R., 1976. Geochemistry of Eocene calc-alkaline volcanic rocks in the Kastamonu area, Northern Turkey. Contrib. Mineral. Petrol. 58, 63–81.
Romer, R.L., 1994. Geochronology of the Kiruna iron ores and hydrothermal alterations. Econ. Geol. 89, 1249–1261.
Seo, J., Choi, S.G., Oh, C.W., 2010. Petrology, geochemistry, and geochronology of the post-collisional Triassic mangerite and syenite in the Gwangcheon area, Hongseong Belt, South Korea. Gondwana Res. 18, 479–496.
So, C.S., 1978. Geochemistry and origin of amphibolite and magnetite from the Yangyang iron deposit in the Gyeonggi metamorphic complex, Republic of Korea. Mineral. Deposita 13, 105–117.
So, C.-S., Kim, S.-M., Son, D.-S., 1975. Origin of the magnetite-bearing amphibolites from the Yangyang iron mine, Korea: new geochemical data and interpretation. J. Korean Inst. Min. Geol. 8, 175–182.
Song, K.Y., Park, S.I., Cho, D.R., 2011. Geological report of Sokcho-Yangyang Sheet 1: 50,000, Korean Institute of Geoscience and Mineral Resources, Daejeon, Korea.
Steiger, R., Jäger, E., 1977. Subcommission of geochronology: convention on the use of decayconstants in geo- and cosmo-chronology. Earth Planet. Sci. Lett. 36, 359–362.
Sun, S.S., McDonough, W.F., 1989. Chemical and isotopic systematic of oceanic basalt: implications for mantle composition and process. In: Saunders, A.D., Norry, M.J. (Eds.), Magmatism in the Ocean Basins: Geol. Soc. Lond. Spec. Publ 42, 528–548.
Sylvester, P.J., Eggins, S.M., 1997. Analysis of Re, Au, Pd, Pt and Rh in NIST glass certified reference materials and natural basalt glasses by laser ablation ICP-MS. J. Geostand. Geoanal. 21, 215–229.
Torab, F.M., Lehmann, B., 2007. Magnetite–apatite deposits of the Bafq district, Central Iran: apatite geochemistry and monazite geochemistry. Mineral. Mag. 71, 347–363.
Valley, P.M., Hanchar, J.M., Whitehouse, M.J., 2011. New insights on the evolution of the Lyon Mountain Granite and associated Kiruna-type magnetite–apatite deposits, Adirondack Mountains, New York State. Geosphere 7, 357–389.
Williams, I.S., 1998. U–Th–Pb geochronology by ion microprobe. In: Mckibben, M.A., Shanks, W.C.I.I., Ridley, W.L. (Eds.), Applications of microanalytical techniques to understanding mineralizing processes. Review in Economic Geology 7, pp. 1–35.
Williams, I.S., Claesson, S., 1987. Isotopic evidence for the Precambrian provenance and Caledonian metamorphism of high grade paragenesis from the Seve Nappes, Scandinavian Caledonides. II. Ion microprobe zircon U–Th–Pb. Contrib. Mineral. Petrol. 97, 205–217.
Williams, P.J., Barton, M.D., Johnson, D.A., Fontbote, L., De Hallar, A., Geordie, M., Oliver, N.H.S., Marschik, R., 2005. Iron oxide copper–gold deposits: geology, space–time distribution, and possible modes of origin. Econ. Geol. 100th Anniv. Vol., pp. 371–405
Wilson, M., 1989. Igneous Petrogenesis. Unwin Hyman, London (466 pp.).